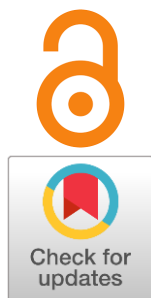


## Field-assisted sintering of refractory oxygen-ion and proton conducting ceramics

Liliya Dunyushkina<sup>a\*</sup>

Received: 15 July 2024  
Accepted: 18 August 2024  
Published online: 29 August 2024

DOI: [10.15826/elmattech.2024.3.040](https://doi.org/10.15826/elmattech.2024.3.040)



Solid oxides with high oxygen-ion and proton conductivity have been extensively studied for applications in electrochemical devices such as fuel cells, electrolyzers, sensors, hydrogen separators, etc. However, the preparation of high-density ceramic electrolytes is often complicated by the exceptional refractoriness of most oxygen-ion conducting solid oxide phases. Therefore, conventional sintering of these materials is very energy consuming and low effective. In recent years, non-conventional field-assisted sintering technologies (FASTs) such as spark plasma sintering, flash sintering and microwave sintering, have been developed and applied for sintering dense ceramic electrolytes at reduced temperatures. In this article, the applications of FASTs for densification of refractory oxygen-ion and proton conducting ceramics are reviewed, while the mechanisms, advantages and limitations of these technologies are discussed, with special emphasis on the effects of FASTs on the microstructural and transport properties of sintered materials, and the performance of FAST-processed electrochemical cells.

**keywords:** solid oxide electrolytes, field-assisted sintering technologies, spark plasma sintering, flash sintering, microwave sintering

© 2024, the Authors. This article is published in open access under the terms and conditions of the Creative Commons Attribution (CC BY) license (<http://creativecommons.org/licenses/by/4.0/>).

### 1. Introduction

Oxygen-ion conducting solid oxides are promising membrane materials for important technological devices such as the solid oxide fuel and electrolysis cells (SOFCs and SOECs) [1, 2], converters of methane to syngas, oxygen pumps, and others. Typical materials from this group, which are currently the most studied and widely used, are zirconia doped with  $Y_2O_3$  or  $Sc_2O_3$  and ceria doped with  $Sm_2O_3$  or  $Gd_2O_3$  [3]. Some oxides demonstrate the proton conductivity in water vapor containing atmospheres. The proton-conducting oxides include the materials with a perovskite structure, among which the most studied are alkaline earth cerates and zirconates [4, 5]. Proton conducting SOFCs and SOECs provide attractive alternatives to the oxygen-ion

conducting systems due to a higher efficiency, lower operating temperatures and reduced cost [6, 7].

The electrolyte membrane separating the fuel and oxidizing gases is an important component of an electrochemical cell. It conducts oxygen ions and/or protons and does not allow electrons to pass through, forcing them to flow in the external circuit. The key requirements to the electrolyte material are the high ionic conductivity combined with the close to zero electron conductivity and high gas-tightness to isolate the fuel and oxidizing gases [8]. However, the fabrication of dense ceramic membranes is complicated by the exceptional refractoriness of most oxygen-ion and proton conducting solid oxides (the melting point is typically above 2500 °C). Conventional solid state sintering of ceria- and zirconia-based electrolytes is usually carried out at the temperatures of 1200–1500 °C [9–13], while proton-conducting BaZrO<sub>3</sub>-based ceramics are to be sintered at 1600 °C and above with a long term exposure [14–17]. Such long-term high-temperature sintering is an energy intensive process.

a: Institute of High Temperature Electrochemistry, Ural Branch of Russian Academy of Sciences, Ekaterinburg 620066, Russia

\* Corresponding author: [Lidung@list.ru](mailto:Lidung@list.ru)

Modification of the conventional sintering by introducing sintering additives, also called as liquid phase sintering, makes it possible to reduce the sintering temperature by several hundred degrees [18–25], but the sintering aids were often found to impair the electrical properties of solid oxide electrolytes [20, 22, 23]. In recent years, new field-assisted sintering techniques (FASTs) such as spark plasma sintering (SPS), flash sintering (FS) and microwave sintering (MS) have gained considerable attention as promising technologies for the processing of materials for SOFCs and SOECs [26–37].

The main difference between FASTs and conventional solid state sintering lies in the heating mechanism. In conventional sintering, heat is produced by an external heat source, and then transferred to the material to be sintered. The heat transfer occurs with large energy losses as heat is easily dissipated. In FASTs, heat is generated inside the material under the influence of an external field, and the heat energy is dissipated directly within the sample. Accordingly, these techniques typically do not require high-temperature furnaces. This makes FASTs energy-saving and advantageous from the environmental and economical points of view technologies. Because of the advantages mentioned above, FASTs have been widely applied for sintering ceramics for various purposes, such as thermoelectric materials, ceramic capacitors, and solid oxide electrochemical cells [35, 38–47].

In this article, the applications of FASTs for the fabrication of dense oxygen-ion and proton conducting ceramics are reviewed, and the mechanisms, advantages and limitations of these technologies are discussed, with special emphasis on the effects of FASTs on the microstructural and transport properties of sintered materials, and the performance of FAST-processed electrochemical cells.

## 2. Spark Plasma Sintering

SPS is based on the combined effect of the applied pulsed direct current and mechanical pressure on the powder material. A powder material is placed into a graphite pressing die and an external pulsed direct electric field is applied as shown in Figure 1. In the case of electrically conductive material, a low applied voltage (typically below 10 V) generates a high current through the sample, resulting in Joule heating, and the produced heat is dissipated directly within the sample. In the absence of ohmic contact at the interfaces between powder particles, electric charge accumulates until a spark discharge occurs, which causes intense short-term heating. In addition, heat is produced in the conductive graphite die and transferred to the powder. A uniaxial pressure is

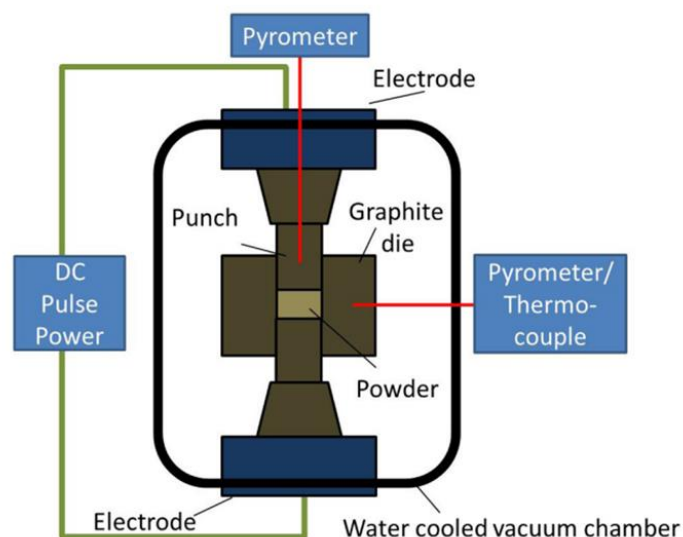


Figure 1 Schematic of SPS apparatus [26].

applied simultaneously with an electric field to enhance the densification process. The amplitude and pulse/pause durations of current can be varied by the modulation of applied voltage. The pulse duration of a few milliseconds and the heating rates of 150–1000 °C · min<sup>-1</sup> are typically used. The process can be carried out in vacuum or at atmospheric pressure in a controlled gas atmosphere. The heated parts are cooled by the water-cooling circuit as shown in Figure 1. The temperature inside the sample is controlled using thermocouples or pyrometers. The temperature as high as 2400 °C can be reached in a graphite die [26].

An important advantage of SPS is that no long-term exposure to elevated temperature is required [48–52]. Due to the high heating rates and short sintering time, the SPS materials typically have the finer grain morphology compared to the conventionally sintered ceramics, which determines the application of SPS for the preparation of nanoceramic and nanocomposite materials [25, 49, 50, 53–55]. Short sintering duration and low temperature help to avoid the evaporation and/or sublimation of volatile components, in contrast to conventional sintering, in which, to preserve the chemical composition, the green compacts are covered with a sacrificial powder of the appropriate composition [56–66], or the compositions with an excess content of volatile components, in particular, barium in Ba-based perovskites, are synthesized [62, 67, 68].

However, this method has a number of limitations, including the problems with scalability and fabrication of ceramics of complex shapes. SPS is more suitable for manufacturing small simple shape forms, since in this case it is easier to ensure the homogeneity of a green compact by uniaxial pressing and thereby the uniform

distributions of current and, accordingly, temperature inside the sample; while the uneven distributions of pressure and current will result in the significant temperature gradients inside the sample and thus non-uniform sintering.

Hocquet et al. [69] adapted the basic SPS technology to densify complex shape ceramic parts, without any modification of the equipment. The novelty of the approach consists in embedding the complex pre-sintered parts in a granular medium that transfers heat and mechanical load. The precursor ceramic powders were compacted by uniaxial pressing and pre-sintered to enhance the mechanical strength so that the green density was about 61 %. Then, the specified shapes were cut out of the pre-sintered samples using conventional or laser machining. The obtained complex shape samples were placed in a powder bed in the classical die used in SPS and sintered.

Another approach to solve the problem of the complex shape ceramics fabrication was suggested by Paygin et al. [70]. The researchers modified the SPS technology by using a specially designed die, which provides the redistribution of friction forces during pressing a powder. In this research, the SPS technology combined with the collector pressing method was used to produce transparent IOYSZ ( $ZrO_2$  stabilized with 10 mol %  $Y_2O_3$ ) ceramics. YSZ is the most common oxide-ion electrolyte used in SOFCs, SOECs and other electrochemical devices [42]. The samples were sintered in a graphite die at a temperature of 1300 °C for 10 min in a vacuum ( $10^{-3}$  Pa) with the heating rates of 15 °C · min<sup>-1</sup> (from room temperature to 1000 °C) and 10 °C · min<sup>-1</sup> (from 1000 to 1300 °C). The powder was pressed using both the conventional uniaxial method and the “collector pressing” method which was patented [71]. The developed method is based on using split dies moving in the opposite direction along the pressing axis during the pressing process. The proposed technology made it possible to obtain the transparent IOYSZ ceramic samples with nearly full density.

Rajeswari et al. [72] reported on the results of comparative study of sintering 8YSZ ( $ZrO_2$  stabilized with 8 mol %  $Y_2O_3$ ) ceramics by the conventional sintering (CS), SPS and MS technologies. The green compacts were obtained by slip-casting of the slurry containing 8YSZ powder; the green densities were in the range of 50–51 % of the theoretical density. In all sintering processes, the sintering parameters were selected in such a way that the density of resultant ceramics was higher than 98 %. CS was carried out at 1500, 1525 and 1550 °C for 2 h, resulting in densities of 98.5, 99.4 and 99.5 %, respectively. The modified CS, so-called two-step sintering (TSS), included

the heating to 1525 °C with no holding time followed by cooling to 1300, 1350 and 1375 °C and holding at these temperatures for 4 h. The TSS samples had the densities of 98.8, 99.4 and 99.5 %, respectively. SPS was conducted under an applied pressure of 50 MPa with a heating rate of 100 °C · min<sup>-1</sup> to the temperatures of 1250 °C and 1325 °C with a holding time of 5 minutes. The obtained density reached 99.1 and 99.5 %, respectively. MS was carried out at 2.45 GHz frequency with a heating rate of 10 °C · min<sup>-1</sup> to the temperatures of 1475 °C, 1525 °C and 1550 °C with a holding time of 15 min. The relative densities of the MS samples were 98.6, 99.2 and 99.2 %. The obtained microstructures, studied by scanning electron microscopy (SEM), are presented in Figure 2. All the samples demonstrated dense microstructures, with the largest average grain size of 4.67 µm in the CS ceramic, and the smallest grains in the SPS sample (1.16 µm). Thus, all sintering technologies were found to be effective for the preparation of dense 8YSZ ceramics; however, the use of FASTs ensured high densification in a significantly shorter time.

SPS was proved to be effective for densification of Ba-containing perovskite materials which are promising proton-conducting electrolytes for SOFCs and SOECs. Bu et al. [73] fabricated the translucent  $BaZr_xCe_{0.8-x}Y_{0.2}O_{3-δ}$  ( $x = 0.5, 0.6, 0.7$ ) ceramics with the relative density of 99 % by SPS at 1350 °C. The authors believe that the low

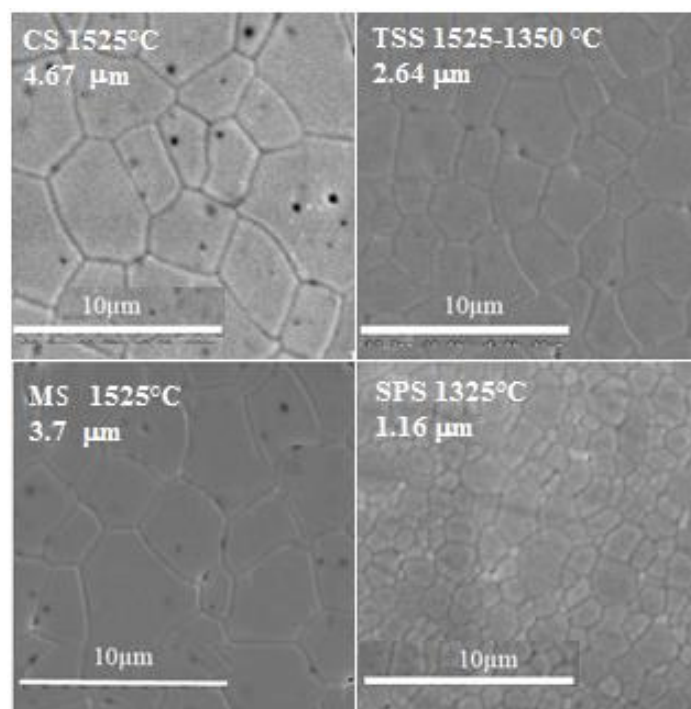


**Figure 2** SEM micrographs of 8YSZ ceramics sintered using conventional sintering (CS), two-step sintering (TSS), microwave sintering (MS) and spark plasma sintering (SPS) technologies. The average grain sizes are given in the micrographs [72].

sintering temperature ( $< 1400\text{ }^{\circ}\text{C}$ ) and fast cooling rate ( $\geq 200\text{ }^{\circ}\text{C}\cdot\text{min}^{-1}$ ) provided so high density of the SPS ceramics.

Maekawa et al. [74] reported on the manufacturing dense (91 % of the X-ray density) ceramic samples of refractory  $\text{BaHfO}_3$  by SPS. The precursor powder obtained by solid state reaction was placed into a graphite die and sintered at  $1500\text{ }^{\circ}\text{C}$  under the argon atmosphere.

Anselmi-Tamburini et al. [75] reported on the use of SPS for the fabrication of dense proton-conducting ceramics of Y-doped  $\text{BaZrO}_3$ . The powders of  $\text{BaY}_x\text{Zr}_{1-x}\text{O}_{3-x/2}$  ( $x = 0, 0.08$  and  $0.16$ ) were synthesized by the wet chemical method and calcined at  $1000\text{ }^{\circ}\text{C}$  for 6 h in the oxygen atmosphere. The precursor powder was poured in a graphite die and heated to  $1400\text{--}1600\text{ }^{\circ}\text{C}$  with a rate of  $200\text{ }^{\circ}\text{C}\cdot\text{min}^{-1}$  by passing a pulsed DC current under an applied pressure of 105 MPa. The holding time at the sintering conditions varied within 0–5 min. The relative density of both undoped and Y-doped  $\text{BaZrO}_3$  ceramics increased with increasing sintering temperature, but the undoped samples were slightly denser; the highest density was as high as 98.5 %. The morphology of sintered ceramics was studied by SEM (see Figure 3). All samples exhibited the nanograined structure with the average grain size increasing from 70–150 nm to 200 nm with the sintering temperature. This research proved that SPS can be used to prepare the high-density proton-conducting  $\text{BaZrO}_3$ -based ceramics at short holding times and low temperatures compared to the conventional solid-state sintering.

Apart from high density, the ion-conducting ceramic membranes should have high conductivity. A number of studies have shown that the SPS ceramics exhibit enhanced conductivity compared to the conventionally sintered samples. For example, Ricote et al. [76] reported the high ionic conductivity of  $\text{BaCe}_{0.9-x}\text{Zr}_x\text{Y}_{0.1}\text{O}_{3-\delta}$  ( $x = 0.3, 0.7, 0.9$ ) ceramics processed by SPS. In this research, the precursor powders were synthesized by the solid state reaction at  $1400\text{ }^{\circ}\text{C}$  for 24 h. The SPS process was performed at  $1600\text{--}1700\text{ }^{\circ}\text{C}$  for 5 min under an applied pressure of 100 MPa. The Ce-free sample was transparent and had the relative density of 99 %, while the Ce-containing samples fell apart after a few days, which was supposed to be caused by the partial reduction of Ce ions in the highly reducing atmosphere formed in the graphite die at high temperature. To identify the effect of SPS processing on the electrical conductivity, the  $\text{BaZr}_{0.9}\text{Y}_{0.1}\text{O}_{3-\delta}$  sample with the relative density of 90 % was prepared by conventional sintering at  $1700\text{ }^{\circ}\text{C}$  for 6 h for comparison. The electrical conductivity of the SPS and CS samples was measured by the DC four-probe method

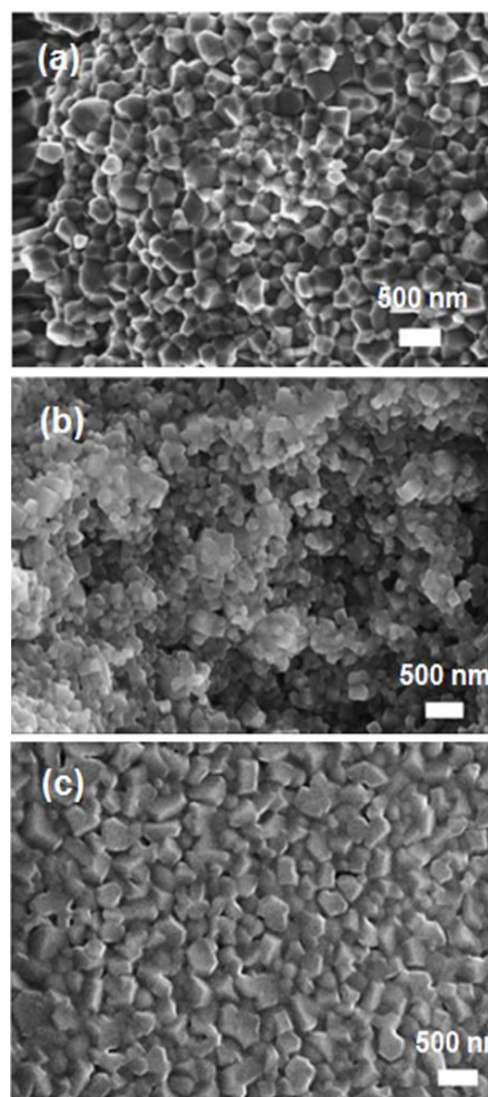


**Figure 3** SEM micrographs of  $\text{BaY}_x\text{Zr}_{1-x}\text{O}_{3-x/2}$  ceramics obtained by SPS at  $1600\text{ }^{\circ}\text{C}$ : (a)  $x = 0$ , holding time 1 min; (b)  $x = 0.08$ , 4 min; (c)  $x = 0.16$ , 5 min. (a, b) fracture surface; (c) after thermal etching [75].

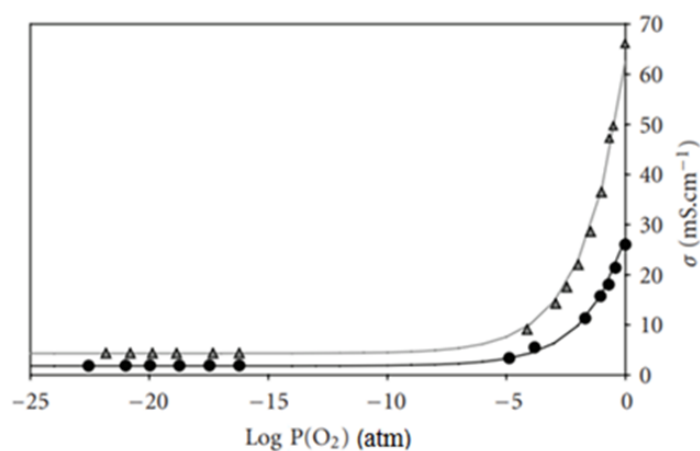


**Figure 4** Electrical conductivity of  $\text{BaZr}_{0.9}\text{Y}_{0.1}\text{O}_{3-d}$  ceramics densified by SPS (triangles) and by conventional sintering (circles) at  $800\text{ }^{\circ}\text{C}$  as a function of oxygen partial pressure [76].

as a function of the oxygen partial pressure (Figure 4). The conductivity of SPS sample was found to exceed that of the CS sample. The enhanced conductivity was explained by the higher density of SPS ceramics.

The enhanced conductivity of  $\text{BaZr}_{1-x}\text{Ho}_x\text{O}_{3-\delta}$  ( $x = 0.1, 0.2$ ) ceramics densified by SPS was reported in [44]. The precursor powders were synthesized by the flash pyrolysis method and calcined at 1100 °C. The powder was placed in a graphite die and sintered at 1600 °C for 20 min under a pressure of 75 MPa. The relative density of the sintered samples was above 99 %. The cation ratios obtained from the energy-dispersive X-ray spectroscopy (EDX) close to nominal values, indicating no loss of barium during sintering. The electrical conductivity of the samples was measured by the impedance method in air and in humidified  $\text{O}_2$  atmosphere ( $p_{\text{H}_2\text{O}} = 0.03$  atm). The conductivity increased with increasing Ho concentration and  $p_{\text{H}_2\text{O}}$ , indicating increasing concentration of oxygen vacancies and significant proton transport.  $\text{BaZr}_{0.8}\text{Ho}_{0.2}\text{O}_{3-\delta}$  composition demonstrated the highest conductivity of about  $49 \text{ mS} \cdot \text{cm}^{-1}$  at 700 °C in humidified  $\text{O}_2$  atmosphere ( $p_{\text{H}_2\text{O}} = 0.03$  atm), which exceeded the conductivities of the conventionally sintered Y-doped  $\text{BaZrO}_3$  ceramics. This was explained by the nearly full density of SPS ceramics.

Highly dense (above 98 %) nanocrystalline  $\text{BaZr}_{0.92}\text{Y}_{0.08}\text{O}_{3-\delta}$  ceramics obtained by SPS also demonstrated high electrical conductivity [77]. The precursor nanopowder synthesized by Pechini technique was heated in a graphite die up to 1400–1500 °C under an applied uniaxial pressure of 100 MPa and exposed to these conditions for 5 min. The resultant ceramics had a grain size of about 85 nm as determined by SEM. The conductivity of highly dense  $\text{BaZr}_{0.92}\text{Y}_{0.08}\text{O}_{3-\delta}$  nanoceramics was measured by the 2-probe impedance method in the wet nitrogen atmosphere and compared with that of a ceramic sample of the same composition with grains of about 1  $\mu\text{m}$  and a density of 94 %, which was sintered conventionally at 1700 °C for 20 h. In the both nano- and microceramic samples, the charge transfer was found to be hindered by grain boundaries; however, in the nanocrystalline samples, the conductivity of grain boundaries was 4 or more orders of magnitude less than that of grain bulk, while in the case of the conventionally sintered ceramic samples the difference reached more than 6 orders. At the same time, the bulk conductivity was nearly independent of the grain size. A significant enhancement in the grain boundary conductivity of the nanocrystalline ceramics resulted in a higher total conductivity. It was suggested that as the grain size decreases to the nanometer range, the nature of grain

boundaries changes, which makes the nanocrystalline  $\text{BaZr}_{0.92}\text{Y}_{0.08}\text{O}_{3-\delta}$  a promising proton-conducting electrolyte for SOFC applications.

However, there are studies that have found a deterioration in the conductivity of SPS processed samples. For example, Wang et al. [43] reported that  $\text{BaZr}_{0.9}\text{Y}_{0.1}\text{O}_{3-\delta}$  nanoceramics sintered by SPS had a lower electrical conductivity than the conventionally sintered samples. The samples were obtained from the  $\text{BaZr}_{0.9}\text{Y}_{0.1}\text{O}_{3-\delta}$  nanopowder synthesized by Pechini technique. The SPS process was carried out at 1300 and 1400 °C for 5 min. The density of resulting ceramics was found to increase from 85.5 % to 92.4 % with sintering temperature, and the average grain size increased from ~200 nm to ~260 nm, respectively. The electrical conductivity of nanoceramics was studied using the impedance spectroscopy method in the temperature range of 300–750 °C. The sample sintered at 1400 °C exhibited a slightly higher conductivity than that sintered at 1300 °C, which can be explained by a larger grain size and a higher density of the former. Nonetheless, the conductivity of both samples was low and the activation energy was high (1.34 and 1.64 eV for the bulk and grain boundary conductivities, respectively, in wet air) compared to the values reported for the conventionally sintered  $\text{BaZr}_{0.9}\text{Y}_{0.1}\text{O}_{3-\delta}$  materials. It was supposed that the nanocrystalline structure of the SPS samples was responsible for the deterioration in conductivity.

Park et al. [78] investigated the electrical conductivity of Y-doped  $\text{BaZrO}_3$  nanoceramics densified by SPS. The precursor nanopowder of  $\text{BaZr}_{0.9}\text{Y}_{0.1}\text{O}_{3-\delta}$  was synthesized by sol-gel method and processed by SPS under the uniaxial pressure of 100 MPa at 1400 °C for 5 min. The relative density of resultant ceramic was 94 % and the average grain size was about 90 nm. The electrical conductivity of the samples was measured in wet air using the 2-probe impedance method. The conductivity was found to increase with increasing  $p_{\text{H}_2\text{O}}$ , that proves the proton contribution. The charge transport was limited by grain boundaries, which indicates that the fine-grained structure of SPS ceramics is unfavorable for conductivity.

Wallis et al. [79] prepared the  $\text{BaZr}_{0.7}\text{Ce}_{0.2}\text{Y}_{0.1}\text{O}_{3-\delta}$  ceramics with the relative density as high as 99.7 % by SPS at 1550 °C for 5 min, under the applied pressure of 80 MPa. The investigation of the sample composition by the EDX method showed that the cation ratios were close to the nominal stoichiometry, despite the high sintering temperature. As the SEM study has shown, the grain size in the sintered ceramics varied from 100 nm to 1.1  $\mu\text{m}$ , with the majority of grains of 300–600 nm. The impedance study revealed that the conductivity of ceramics was

limited by resistive grain boundaries; the total conductivity was about  $0.26 \text{ mS} \cdot \text{cm}^{-1}$  at  $600 \text{ }^\circ\text{C}$  in the  $3 \text{ } \%$   $\text{H}_2\text{O} + 5 \text{ } \%$   $\text{H}_2/\text{Ar}$  atmosphere. Thus, for the fabrication of proton-conducting ceramics using SPS, the optimization of sintering process parameters is required to enhance grain growth and, accordingly, the ionic conductivity.

Simonenko et al. [80] obtained the lower conductivities of  $\text{BaCe}_{0.9-x}\text{Zr}_x\text{Y}_{0.1}\text{O}_{3-\delta}$  ( $x = 0, 0.5, 0.6, 0.7$  and  $0.8$ ) ceramics densified by SPS compared to the similar compositions reported in other research studies. The SPS samples were obtained from the nanopowders synthesized by citrate-nitrate process. SPS was conducted at a temperature of  $900 \text{ }^\circ\text{C}$  and a holding time of 5 min. The SEM study showed that the average grain size decreased with increasing Zr concentration from 150 nm in the Zr-free composition to about 80 nm at  $x = 0.5$ . The relative density of Zr-free sample was as low as 70 % and further decreased to 60 % for the Zr-containing ones. The low density was most likely a result of the low sintering temperature: dense SPS ceramics were obtained at much higher temperatures in other studies [43, 44, 72–78].  $\text{BaCe}_{0.4}\text{Zr}_{0.5}\text{Y}_{0.1}\text{O}_{3-\delta}$  solid solution was found to have the highest conductivity ( $\sim 0.3 \text{ mS} \cdot \text{cm}^{-1}$  at  $550 \text{ }^\circ\text{C}$  in ambient air) among the series, which, nevertheless, was much lower than the conductivity of the denser ceramics of similar composition. The  $\text{BaZr}_{0.1}\text{Ce}_{0.7}\text{Y}_{0.1}\text{O}_{3-\delta}$  ceramic with a density of about 98 % was reported to have a conductivity of  $\sim 6 \text{ mS} \cdot \text{cm}^{-1}$  at  $550 \text{ }^\circ\text{C}$  in wet air (3 %  $\text{H}_2\text{O}$ ) [81], while the conductivity of  $\text{BaZr}_{0.7}\text{Ce}_{0.2}\text{Y}_{0.1}\text{O}_{3-\delta}$  nanoceramics with a density of 96 % was as high as  $\sim 8 \text{ mS} \cdot \text{cm}^{-1}$  at  $550 \text{ }^\circ\text{C}$  in wet air (2.5 %  $\text{H}_2\text{O}$ ) [82]. The low conductivity of  $\text{BaCe}_{0.9-x}\text{Zr}_x\text{Y}_{0.1}\text{O}_{3-\delta}$  ceramics obtained in [80] is most likely caused by its low density.

Thus, the SPS processed ceramics typically exhibit dense fine-grained microstructure, and nearly full density was obtained in some studies [44, 75, 77, 79]. A high density of SPS ceramics is beneficial for the electrical conductivity [44, 45, 77]. In the fabrication of ceramics containing volatile components, a low sintering temperature and a short holding time are the valuable advantages [44, 79]. So, SPS can be considered as a promising technique for the rapid densification of oxygen-ion and proton-conducting ceramics at low temperatures, although optimization of sintering process parameters is required to enhance grain growth and electrical conductivity.

### 3. Flash Sintering

FS is the electric field assisted process, similar to SPS. However, these methods have several differences. First, FS is based on applying high voltage, and no pressure is typically applied to the green ceramic powder compact, unlike SPS. The compacted green bodies with the relative density of 50–55 % of the theoretical density are hanged in a furnace by two metallic wires which act simultaneously as electrodes, as described e.g. in [83], or placed between two alumina supports as reported in [84]. Other possible geometries of a sample and metallic electrodes used in FS are considered in [85]. While both electrically conductive and non-conductive materials can be processed by SPS, the ionically conducting or semiconducting materials should be used in FS. A high electric field applied during sintering results in the sample densification at lower temperatures and shorter times compared to SPS due to the enhanced ion transport and grain boundary diffusion at elevated temperatures. In contrast to SPS, which is based on passing pulsed direct current through the sample, direct current or high frequency alternating current is used in the case of FS.

Another difference of FS is that the powder compacts to which an electric field is applied should be slowly heated. Fast sintering, or so-called “flash event”, occurs when a certain critical temperature called the onset of “flash event” is reached. At this temperature, a sharp increase in current is observed, despite the constant magnitude of the applied voltage [25, 28, 50, 72, 83–86]. After the “flash event” occurs, the voltage control mode is switched to the current control one. In the isothermal mode of FS, an electrical field is applied to a sample which is maintained at a constant temperature [87, 88]. In this case, flash onset is observed after a delay time, which depends on the conductivity of powder compact.

Unlike SPS materials which typically have the fine-grained morphology, the FS ceramics can have both a nano-grained structure and a coarse-grained structure with grain sizes up to several micrometers, depending on the FS process parameters [40, 41, 87, 89, 90]. As in the case of SPS, there are the problems of scalability and manufacturing complex shapes in the FS technology, because the uniform distributions of current and temperature inside the sample must be ensured.

The first report on the use of FS for manufacturing dense solid oxide electrolytes was made in 2010 by Cologna et al. [72]. In this research, a constant voltage was applied to the green compact of zirconia stabilized with 3 mol %  $\text{Y}_2\text{O}_3$  (3YSZ), which was slowly heated in a resistance furnace. After the “flash event” occurred, the specimen sintered to near full density. Later, the use of an

alternating current in FS was reported [91], and different ceramics were produced by this technique [39, 91–94].

Fabrication of dense 8YSZ ( $\text{ZrO}_2$  stabilized with 8 mol %  $\text{Y}_2\text{O}_3$ ) solid oxide electrolyte using FS was reported in [95]. The green pellets were obtained from ceramic powder by the uniaxial and isostatic pressing at 46 MPa and 200 MPa, respectively; the green relative density was about 50 %. To improve the contact with electrodes, the pellet faces were covered with Pt paint. The sample was inserted between two Pt foils acting as current collectors. A mechanical load of a few hundred grams was applied to the assembly to improve the electric contact using springs as shown in the scheme of a sample holder (Figure 5). Then, the sample holder was placed in a furnace. After heating the sample, a DC or AC voltage was applied and the evolution of current in time was studied. Besides, the sample impedance was measured during the processing. A typical dependence of current on time during flash sintering, which was recorded under the applied voltage of 8 V at 1000 Hz frequency at 970 °C, is shown in Figure 6. As can be seen, the current is small and remains nearly stable during the first ~30 s, then it increases abruptly reaching a plateau. After decreasing the applied voltage, the current falls down. The density of the FS sample, which was determined by the Archimedes method, was 94 % of theoretical density. SEM study of the polished surface of FS sample showed its nanograined structure (Figure 7). The resistance of the sintered sample, measured by the impedance method, became 11 times less than before processing due to the improved density. The electrical conductivity of the FS processed 8YSZ reached  $0.17 \text{ mS} \cdot \text{cm}^{-1}$  at 420 °C, which is comparable with the conductivity of ceramics of the same composition with an average grain size of 18  $\mu\text{m}$ , prepared by the conventional solid state sintering at 1700 °C for 12 h, equaled to  $0.14 \text{ mS} \cdot \text{cm}^{-1}$  at 420 °C [96].

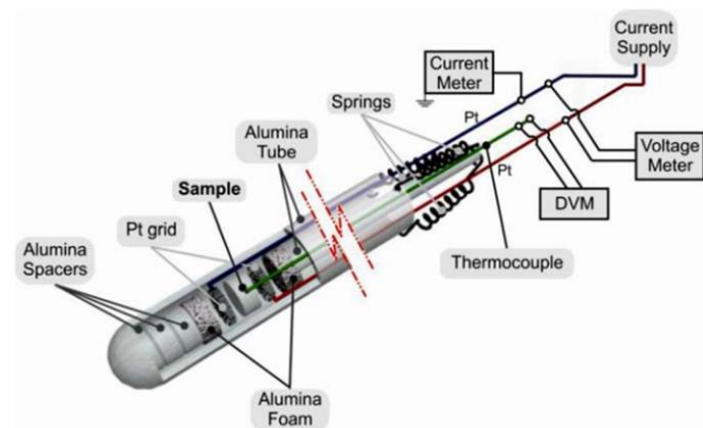


Figure 5 Scheme of sample holder [95].

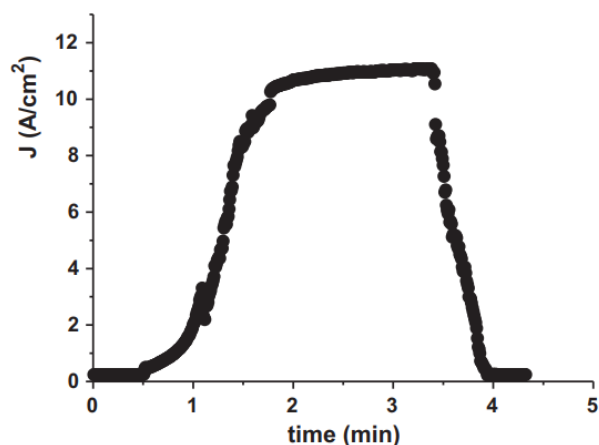


Figure 6 Current versus time curve during FS processing of 8YSZ at 970 °C under applied AC voltage of 8 V, 1000 Hz [95].

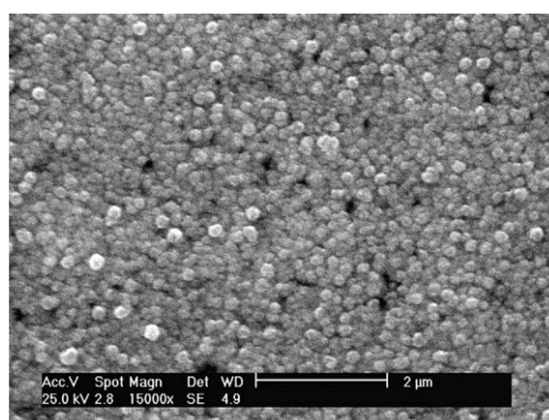


Figure 7 Scanning electron microscopy image of polished surface of flash sintered 8YSZ [95].

Du et al. [89] analyzed the microstructure and electrical conductivity in the flash and conventionally sintered 8YSZ ceramics. The powder of 8YSZ was uniaxially pressed into pellets (9.5 mm in diameter and 5 mm thick) at a pressure of 1 MPa followed by isostatic pressing at 200 MPa. The green density was 50 % of the theoretical density. The FS process was carried out in a dilatometer by heating to 1500 °C with a rate of  $10 \text{ }^\circ\text{C} \cdot \text{min}^{-1}$  followed by cooling at  $20 \text{ }^\circ\text{C} \cdot \text{min}^{-1}$ . A green pellet was placed between two Pt electrodes (2 mm thick) with polished surfaces, and a mechanical load of 7 kPa was applied to improve the electrode/sample contacts. A constant electric field of  $50 \text{ V} \cdot \text{cm}^{-1}$  was applied during heating. The flash sintering was interrupted when the sample shrank for 5, 10, 15 and 20 % (the samples were marked as F5 %, ..., F20 %). An additional sample, labeled as LF20 %, was prepared by applying voltage for 5 min after reaching 20 % shrinkage. For comparison, a similar set of the conventionally sintered at 1500 °C ceramics were prepared (C5 %, ..., C20 %). It was found

that during conventional sintering, shrinkage started at about 1100 °C and reached a maximum of 20.5 % at 1500 °C, resulting in 99.8 % density during ~ 40 min. In FS processing, shrinkage started below 1070 °C, reaching the maximum density of 95.7 % in ~ 1 min.

The microstructures of the FS and CS ceramics were analyzed using SEM (see Figure 8). In general, the microstructures of the samples after the sintering interruption were similar. After the interruptions at 5 % and 10 % shrinkage, the average grain size of CS samples was slightly higher than that of FS ones, while at 15 % and 20 % shrinkage, the grain size of the FS samples became higher. It was found that the grain size was homogeneous throughout the CS and FS ceramics, except for the LF20 % sample, in which the average grain size at the center was twice as large than near the surface. This was explained by the temperature gradient induced by faster heat dissipation near the surface. In both CS and FS samples, the average grain size remained small (100–150 nm) at the relative densities of up to 80–85 %, and significantly increased (to 1–3 μm) at higher densities. This result contradicts the previously reported conclusions about the inhibited grain growth during flash sintering [30, 31].

The electrical conductivities of the CS and FS samples, determined from the impedance measurements, were similar, which can be explained by the similar densities and microstructures of the samples (Figure 9). As mentioned above, the shrinkage and current of the green sample were found to change abruptly at a relatively low furnace temperature (~ 1070 °C). However, the sample temperature can strongly deviate from the furnace temperature during processing. The estimation of the sample temperature using the black-body equation proved that the conductivity obeys the Arrhenius law during flash sintering as expected for the ionic conductivity in 8YSZ. Flash sintering was concluded to be a process driven by Joule heating. The apparent non-linear dependence of conductivity on temperature at flash onset (see Figure 6, the temperature of a furnace is proportional to time) was supposed to be caused by the higher sample temperature because of Joule heating. Considering the sample temperature, it was concluded that the densification process in FS occurs at the temperature similar to that in conventional sintering.

Francis et al. [97] reported on the particle size effects on flash sintering of 3YSZ ceramics. The 3YSZ powders with the particle sizes of 1, 2, 5 and 10 μm were used as precursors. Dense ceramics (96 % of relative density) were obtained only from the powder with the smallest particle size, while the larger particle size resulted in only 82–84 % density. This was explained by the nucleation and diffusion of Frenkel defects. The lower densities were

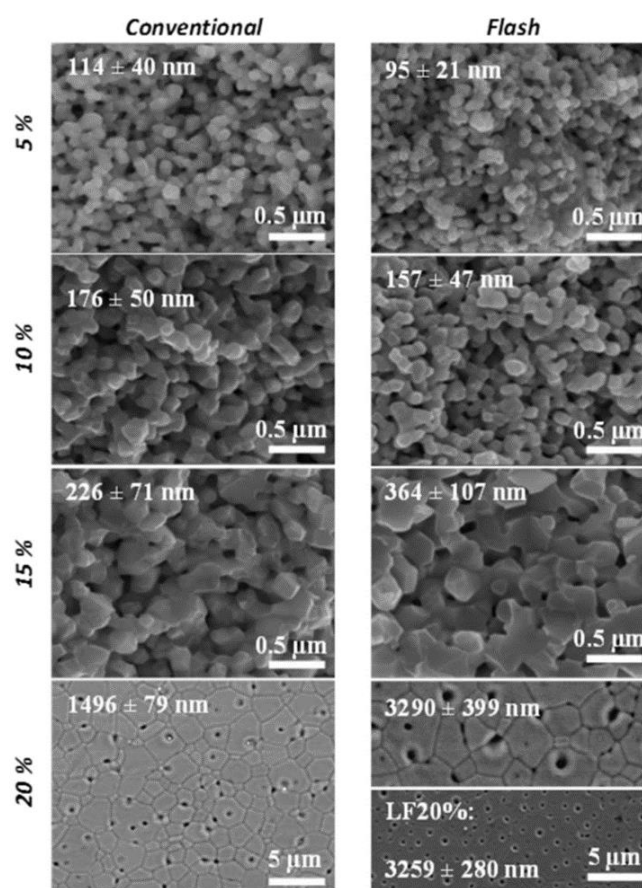


**Figure 8** Microstructure of conventional and flash sintered 8YSZ samples interrupted during thermal cycle at different linear shrinkage values. Average grain size values refer to the center of the samples. LF20 % is the flash sintered sample prepared by applying voltage for 5 min after reaching 20 % shrinkage [89].

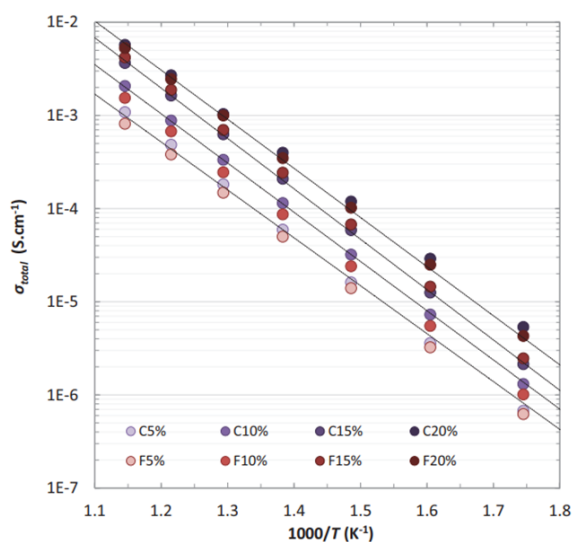


**Figure 9** Arrhenius plots for the total conductivity of conventionally and flash sintered 8YSZ samples with different relative densities. F5 %, ..., F20 % symbols indicate the flash sintered samples with shrinkage of 5, 10, 15 and 20 %; C5 %, ..., C20 % symbols indicate the conventionally sintered samples with shrinkage of 5, 10, 15 and 20 % [89].

attributed to longer diffusion distances in large particles, that requires a longer time for the Frenkel defects to travel to the pores, comparable with the lifetimes of the Frenkel defects. However, the temperature inside the sample can significantly differ from that of a furnace, as was reported in [89]; therefore, the effect of the sample temperature on the resultant density is to be considered in order to make a conclusion about the mechanism of the process.

Caliman et al. [84] designed an experimental setup that made it possible to set and control the atmosphere during FS process and to apply a slight pressure to the sintered sample. Schematic of the setup is shown in Figure 10. In this scheme, a pellet-shaped sample was placed between two platinum disc electrodes and fixed with the help of two alumina supports. The green pellets with a relative density of 50–55 % were obtained by the uniaxial and isostatic cold pressing under 60 and 250 MPa, respectively. To improve the contact with electrodes, the opposite faces of the pellets were painted with a metallic ink. The experimental setup was placed in a uniaxial press to apply a mechanical load when necessary. It was found that the pressure-assisted sintering is more advantageous compared to conventional FS. A quadruple flash sintering of 3YSZ under the pressure of 48 MPa resulted in dense ceramics. SEM investigation of the resulting ceramics showed that they had fine morphology with grains of about 200 nm (Figure 11). The effect of atmosphere on the FS process was demonstrated on  $\text{Al}_2\text{O}_3$  samples with Ag electrodes: the onset of “flash event” was observed at lower temperature in the Ar atmosphere than in air ( $\sim 500^\circ\text{C}$  and  $\sim 850^\circ\text{C}$ , respectively).

Xu et al. [25] also used the pressure-assisted FS technology applying a pressure of 30 MPa during the sintering process. It was found that 3YSZ ceramics can be sintered at lower temperature with lower electric field under the applied pressure: the onset flash temperature was only  $909^\circ\text{C}$  when a DC voltage of  $33\text{ V}\cdot\text{cm}^{-1}$  was applied. The effect of various applied DC voltages ( $0\text{--}67\text{ V}\cdot\text{cm}^{-1}$ ) on the sintering processes was investigated; the temperature of flash event was found to decrease with increasing voltage, which can be explained by the stronger heating of the material when a higher current is passed through it.

The influence of atmosphere on the flash sintering of 8YSZ was studied by Bhandari et al. [98]. The powder of 8YSZ with the average particle size of 155 nm was uniaxially pressed into a dog-bone and pre-sintered at  $900^\circ\text{C}$  for 1 h, resulting in the green density of about 45 %. The green sample was loaded in a vertical tubular furnace with two Pt wires which were connected to a DC

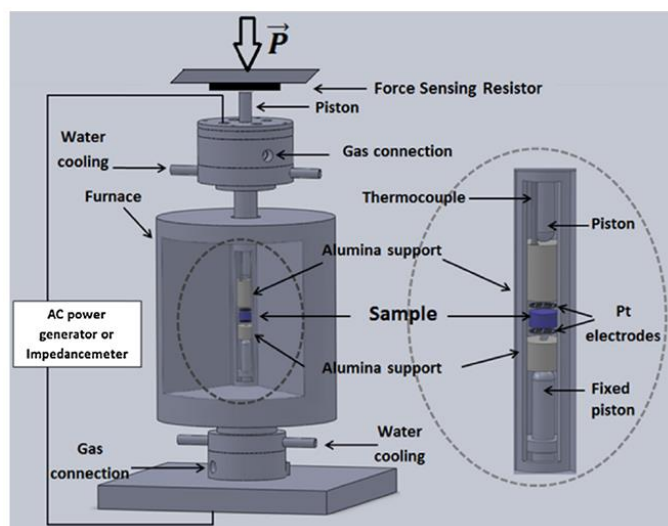


Figure 10 Flash sintering experimental set-up [84].

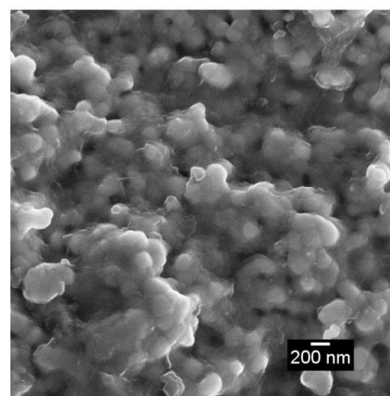


Figure 11 SEM micrograph of flash sintered 3YSZ [84].

power supply. The FS experiments were performed in three different atmospheres: air, Ar and diluted hydrogen ( $\text{Ar} + 2.9\% \text{H}_2$ ). It was found that the flash onset temperature decreases with decreasing oxygen partial pressure ( $p_{\text{O}_2}$ ) in the ambient atmosphere, being equal to  $\sim 825^\circ\text{C}$ ,  $\sim 745^\circ\text{C}$ , and  $\sim 730^\circ\text{C}$  in air, Ar and  $\text{Ar} + 2.9\% \text{H}_2$ , respectively, at the applied DC voltage of  $75\text{ V}\cdot\text{cm}^{-1}$ . The authors explained the observed effect by the enhanced conductivity of 8YSZ in reducing atmospheres due to the formation of oxygen vacancies and electrons; the higher current density results in the generation of more Joule heat inside the sample. The result confirms that Joule heating is one of the main factors in FS.

Steil et al. [87] studied the influence of limiting current which was controlled by the applied AC voltage and the furnace temperature during flash sintering on the microstructure of 8YSZ ceramics. The precursor 8YSZ powder with 30 nm particle size forming the agglomerates of  $15\text{--}140\ \mu\text{m}$  was used. The powder was uniaxially and isostatically cold pressed into pellets (8 mm in diameter and 2 mm thick) under 100 and 250 MPa, respectively,

resulting in green densities of about 50 %. Pt grids were slightly pressed against the pellet faces to serve as current collectors. AC voltage of 0–115 V with a frequency of 1000 Hz, was applied to the sample, while the resulting alternating electric current was limited by a value of 15 A. The applied electric field induced an abrupt current rise after a delay period, which resulted in the sample densification. It was found that the magnitude of limiting current has a strong effect on the ceramic microstructure. SEM micrographs of the samples sintered at different currents at the furnace temperature of 900 °C show that the microstructures are similar at the current densities of 0.3–3 A · cm<sup>-2</sup>, while the grain size strongly increases with increasing current to 6 A (Figure 12). Considering the SEM images, it was concluded that the current density higher than 6 A · cm<sup>-2</sup> is needed for obtaining high-density 8YSZ ceramics.

Variation of the furnace temperature was also found to strongly affect the densification of ceramics. Figure 13 presents the SEM micrographs of the samples sintered under the limiting current of 6 A at the different furnace temperatures (800, 900 and 975 °C). The highest temperature promoted the better densification: the sample had the geometrical and Archimedes densities of 94 % and 97 %, respectively.

However, after sintering at high limiting currents and furnace temperatures, the microstructure of sintered samples was heterogeneous, with large grains at the center and smaller grains near the surface. Such microstructure is similar to that of the sample kept for 5 min under the flash conditions, described in [89]. The formation of the heterogeneous microstructures in both works was explained by the dissipation of supplied power from the sample surface. To avoid such heterogeneities, a short exposure to high limiting currents was recommended. Another problem observed in the samples at high current densities was the appearance of microcracks, which indicated the grain cohesion weakening under severe flash conditions. This research demonstrates that the required microstructure of ceramics can be obtained by appropriate selecting the parameters of flash sintering.

Muccillo et al. [91] prepared dense proton-conducting BaCe<sub>0.8</sub>Gd<sub>0.2</sub>O<sub>3-δ</sub> ceramics by FS from the precursor powder synthesized by the solid state reaction method. The powders were uniaxially and then isostatically pressed into pellets under 30 MPa and 200 MPa. The green density of the compacts was 35–40 %. The pellet faces were painted with Pt paste and calcined at 500 °C. The sample was inserted in a holder between two platinum meshes connected to the power supply or impedance analyzer and heated to ~ 910 °C to decrease the sample resistance to about 10 Ohms. Then, an AC voltage was

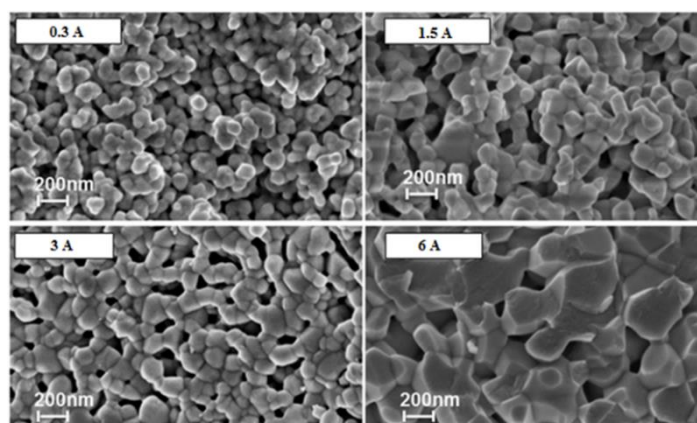


**Figure 12** Influence of the current density on microstructure of the flash sintered 8YSZ ceramics. Furnace temperature 900 °C [87].

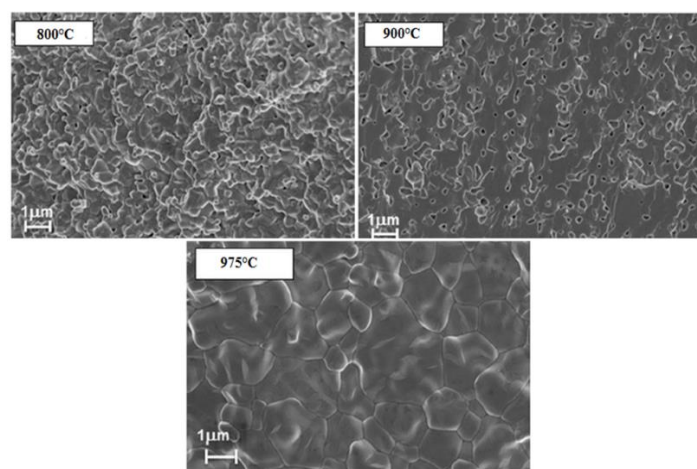


**Figure 13** Influence of the furnace temperature on the microstructure of 8YSZ ceramics at constant current density (6 A · cm<sup>-2</sup>) [87].

applied until the flash event occurred and switched off after that to avoid an avalanche current which could melt the specimen. After sintering, the sample was cooled down to an intermediate temperature, at which the conductivity measurements by the impedance method were carried out. The FS samples had a relative density of 84 %. For comparison, the sample of the same composition was conventionally sintered at 1600 °C for 4 h. The impedance spectra were similar for the CS and FS samples, which indicated that they had similar microstructure and density.

Jiang et al. [40] reported on the fabrication of proton-conducting BaZr<sub>0.1</sub>Ce<sub>0.7</sub>Y<sub>0.1</sub>Yb<sub>0.1</sub>O<sub>3-δ</sub> (BZCYYb) ceramics by the DC flash sintering from the powder prepared by sol-gel method. The precursor powder was mixed with 5 wt % PVA binder in aqueous solution and uniaxially pressed into bars (20 mm × 1.6 mm × 6.5 mm) under a pressure of 500 MPa. Then, platinum wires were wounded at the bar ends as electrodes, and the contacts

were additionally coated with platinum paste to improve the distribution of an electric field through the bar. The sample was placed in a tubular furnace, heated to 850 °C with a rate of 10 °C · min<sup>-1</sup> under the applied constant DC voltage and exposed to the flash conditions for 1 h. To prevent an excessive increase of current density which could result in the fracture of ceramics, the power supply was switched to the current control mode after the onset of flash-sintering. It was found that the “flash event” in BZCYYb sample occurred at a certain furnace temperature, which increased with decreasing applied voltage being equal to 828 °C, 792 °C and 670 °C under 60 V · cm<sup>-1</sup>, 70 V · cm<sup>-1</sup> and 80 V · cm<sup>-1</sup>, respectively. The onset temperature for BZCYYb was higher than that for the Gd-doped ceria in similar flash conditions [99], which can be explained by a lower ionic conductivity of BZCYYb. SEM study of the sintered ceramics showed that porous structures were obtained at low limiting current (< 5 A · cm<sup>-2</sup>); while at higher currents, well-densified structures were observed (Figure 14). The average grain size significantly increased with increasing current density.

Based on these results, it was concluded that the current magnitude plays a key role in the DC flash sintering. The intensive densification and an increase in grain size with the current density was related to Joule heating at grain boundaries. The conductivity of the sintered samples measured using the impedance method was found to increase with the limiting current as shown in Figure 15, which can be explained by the higher density and coarser grains in the samples sintered at a higher current density. This research demonstrates that the dense proton-conducting BZCYYb ceramics with designed grain size and microstructure can be obtained by the DC flash sintering with the adjusted values of current density and dwell time, at the temperature as low as 850 °C, for 1 h.

Soleimany et al. [41] investigated the effect of NiO additions on the sinterability of BaZr<sub>0.1</sub>Ce<sub>0.7</sub>Y<sub>0.2</sub>O<sub>3-δ</sub> (BZCY7) ceramics processed by FS. The powder of BZCY was synthesized by the solid-state reaction method and mixed with 0.5, 1, 1.5, and 2 wt % NiO powder by ball-milling in ethanol. The obtained powders were uniaxially pressed at 180 MPa and machined into the dog-bone shape samples. The sample was suspended into the center of a tubular furnace with the help of nickel wires, which simultaneously served as electrodes. Then, the sample was heated with a rate of 10 °C · min<sup>-1</sup> under an applied DC voltage of 100–500 V · cm<sup>-1</sup>. The DC voltage was adjusted so that the current density across the specimens did not exceed 10 A · cm<sup>-2</sup>. The sample was kept for 40 s at the flash sintering conditions.

It was found that the additions of 0.5 and 1 wt % NiO resulted in a lower onset temperature of flash sintering

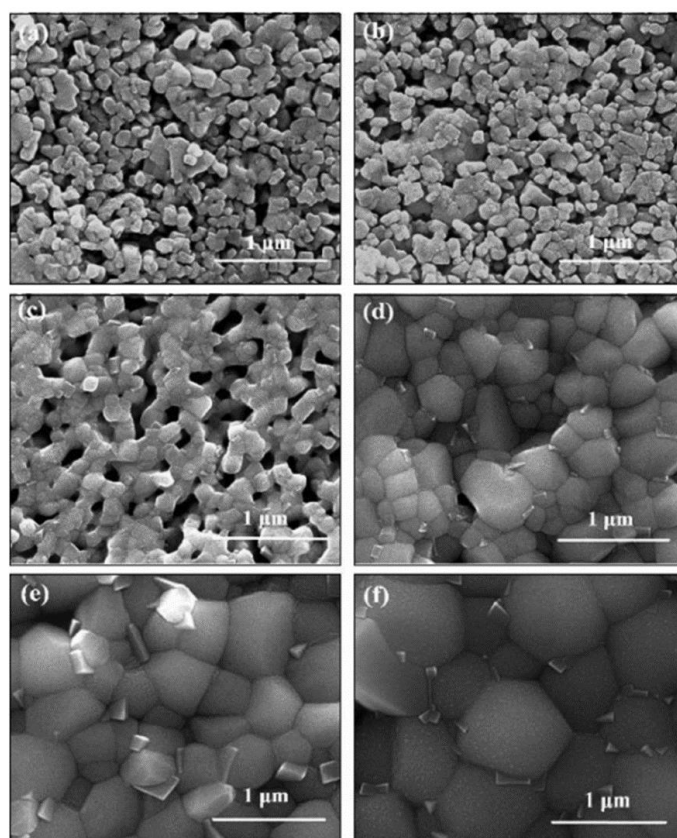


**Figure 14** SEM micrographs of the surface of BZCYYb ceramics sintered at different current densities: (a) no current applied, (b) 1 A · cm<sup>-2</sup>, (c) 3 A · cm<sup>-2</sup>, (d) 5 A · cm<sup>-2</sup>, (e) 7 A · cm<sup>-2</sup>, (f) 9 A · cm<sup>-2</sup> [40].

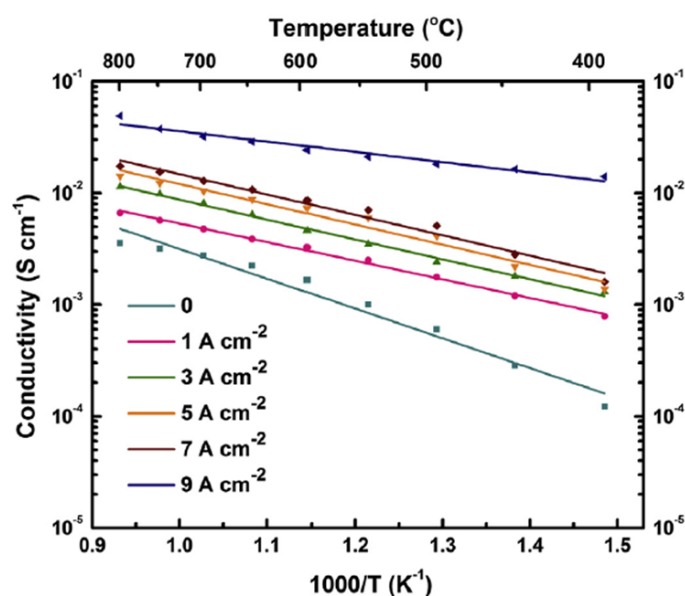


**Figure 15** Total conductivity of BZCYYb ceramics sintered at different current densities [40].

due to the higher internal heating. The samples with 1.5 and 2 wt % NiO not only showed a lower power dissipation, but also star-shaped cracks along the current flow direction appeared in them. This could be caused by

the uneven distribution of the current density and thus the temperature gradients inside the sample. The magnitude of applied DC voltage was found to strongly affect the microstructure of resultant ceramics. SEM images of the fracture surfaces of BZCY7-0.5 % NiO samples flash sintered at different voltages are presented in Figure 16.

The average grain size reached a maximum value of about  $5.5 \mu\text{m}$  at  $200 \text{ V} \cdot \text{cm}^{-1}$ , decreasing with a further increase in voltage. The sample temperature, estimated using the black-body equation, did not significantly depend on the applied electric field, varying within  $1650\text{--}1720 \text{ }^\circ\text{C}$  with a minimal value at  $200 \text{ V} \cdot \text{cm}^{-1}$ , at which the largest grains were observed. The reasons for such effect of the applied voltage on the microstructure of resultant ceramics are not entirely clear: in conventional sintering, the higher temperature typically results in

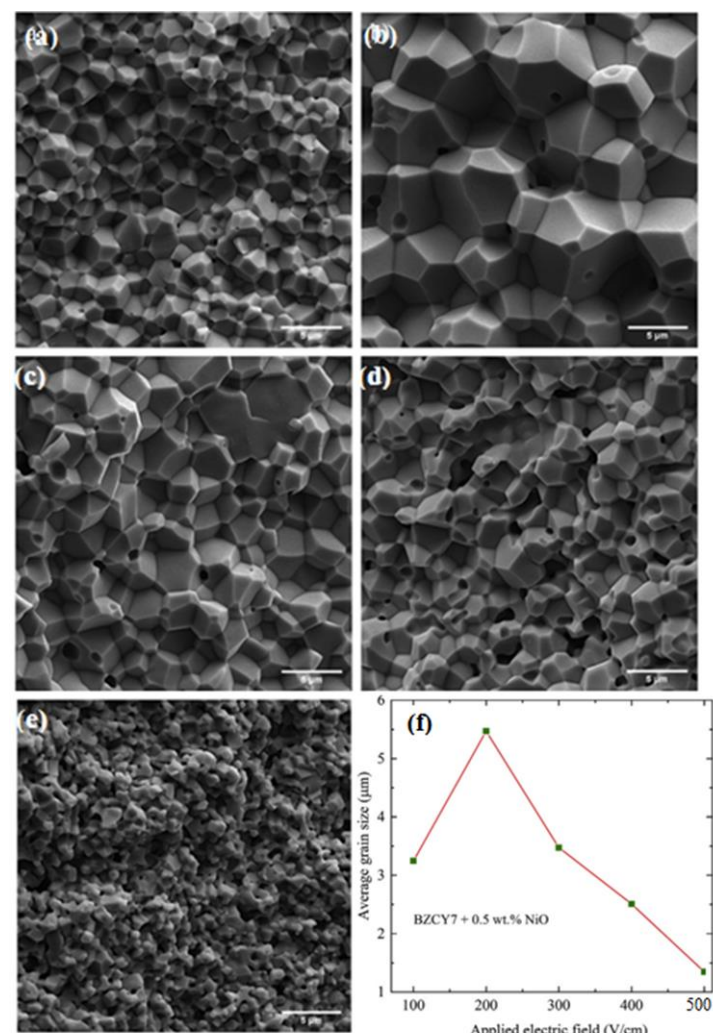


**Figure 16** SEM micrographs of fracture surfaces of BZCY7-0.5 % NiO samples, flash sintered under applied electric fields of (a) 100, (b) 200, (c) 300, (d) 400, and (e)  $500 \text{ V} \cdot \text{cm}^{-1}$ , and the average grain size vs applied electric field (f) [41].

larger grains. The comparison of linear shrinkages of the Ni-free BZCY7 sample, which was studied in [100], and BZCY7 with 0.5 % NiO during flash sintering showed that the addition of NiO resulted in a stronger shrinkage at all applied voltages, which indicated that NiO enhances the flash-sinterability of BZCY7. In addition, the electrical conductivity of the NiO-modified sample was higher than that of the Ni-free composition.

Despite the high research activity in the field of FS processing of ceramics, the mechanism of flash sintering remains controversial [28–30, 83, 101]. R. Raj suggested that a very high temperature developed within the sample during FS process ( $\sim 1900 \text{ }^\circ\text{C}$ ) is responsible for sintering [28]. Todd et al. [83] supposed that the thermal and electric characteristics of flash sintering are a consequence of the negative temperature coefficient of the material resistivity leading to runaway Joule heating at a constant applied voltage. The Joule heating during the “flash event” was assumed to be responsible for the rapid sintering in a number of research studies (e.g. [89, 98, 101]). On the other hand, Naik et al. [30] believe that the nucleation and growth of new defect structures due to extremely high temperatures cause the “flash event”. Francis et al. [97] reported that the temperature in a sample during flash sintering is about  $1200 \text{ }^\circ\text{C}$ , which is well below the estimated temperature of  $\sim 1900 \text{ }^\circ\text{C}$ ; and accordingly, Joule heating cannot explain the flash event. Based on the simulation results on the temperature distribution during FS, Wang et al. [102] concluded that the rapid densification was related to the high heating rate ( $2000\text{--}3000 \text{ K} \cdot \text{min}^{-1}$ ) generated inside the sample.

Despite the incomplete understanding of the mechanisms of the process, FS has been widely applied for sintering of ceramics for various purposes including solid oxide electrolytes. The results presented in the literature show that FS is an effective method for manufacturing dense ceramics from refractory oxide-ion and proton-conducting solid oxides. The main advantage of FS is the ability to densify materials in a short time, without the use of high temperature furnaces. However, the fabrication of ceramics is influenced by many factors, including the atmosphere composition, temperature, applied voltage, current density, and mechanical load application. Therefore, the fabrication of high-density oxygen-ion and proton-conducting ceramics with the desired microstructure requires the systematic optimization of the FS parameters.

#### 4. Microwave Sintering

The heating mechanism in MS as well as in SPS and FS differs from that in the conventional sintering technology.

MS employs electromagnetic waves to heat the powder to be sintered. The absorbed electromagnetic energy is converted into the thermal energy inside the material, which provides fast heating. The heating mechanism of dielectric materials due to the microwave radiation is shown in Figure 17. The key advantages of MS are the fast processing, reduced sintering temperature and holding time, low energy consumption and environmental hazards [32, 36, 37, 103–105]. MS allows high densification of a powder in just a few minutes at the temperatures which are several hundred degrees below the conventional sintering temperature [106]. The low processing temperature restrains the grain growth, which results in the fine-grained morphology of MS ceramics.

While the MS technology has brought about important advancements, it also has some drawbacks. The problem with scalability of microwave-assisted sintering of ceramics is one of the most significant. Furthermore, the precursor powder must meet certain requirements. For efficient sintering, the powder particle size should not exceed the penetration depth of the microwave radiation. The advancements and limitations of the microwave sintering of ceramics have been summarized in a number of review papers, e.g. [32–34].

The microwave processing of refractory materials started in 1960s, while the feasibility of MS for the densification of solid oxide such as alumina, zirconia, and yttria was reported in 1980s [33]. The advantages of MS for densification and electrochemical properties of solid oxide electrolytes have been demonstrated in many studies. In 2005, Vanetsev et al. [107] employed MS for preparation of dense  $\text{BaCeO}_3$  ceramics at the temperature as low as  $900\text{ }^\circ\text{C}$ . This research proved that MS is a promising technology for fabrication of dense proton-conducting electrolytes in a short time at a relatively low temperature.

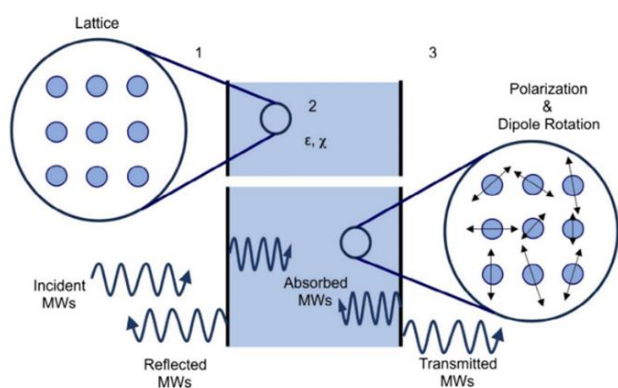


**Figure 17** Heating mechanism of ceramic dielectrics due to microwaves (MWs) – ceramic interaction when MWs are 1) incident on the ceramics with a fraction getting reflected, 2) absorbed, and 3) the rest transmitted [32].

Amiri et al. [108] fabricated the tubular Ni-YSZ cermet supported fuel cell with a thin 8YSZ electrolyte, which was densified by the MS technology, and compared the electrochemical performance of this cell with that of a similar cell except the electrolyte layer was sintered conventionally. For the support fabrication, the powders of YSZ and NiO taken in 35 : 65 weight ratio were ball milled for 24 h in an aqueous medium and mixed with 30 vol. % graphite. The NiO-YSZ tubes were formed by slip casting and pre-sintered at  $1000\text{ }^\circ\text{C}$  for 3 h. In case of MS processing, the tubes were reduced at  $750\text{ }^\circ\text{C}$  for 3 h in a flow of  $\text{N}_2 + 20\text{ vol. } \% \text{ H}_2$ . To prepare the electrolyte layer, the suspension consisting of a mixture of 8YSZ powder, ethanol and 6 wt % ethyl cellulose in terpineol used as a binder was prepared and deposited on the Ni-YSZ supports by dip-coating. The electrolyte layer was sintered in a microwave furnace. For comparison, the identical Ni-YSZ supported half-cell was conventionally sintered (CS) at  $1400\text{ }^\circ\text{C}$  for 3 h. Then, the cathode layer of  $\text{La}_{0.6}\text{Sr}_{0.4}\text{Co}_{0.2}\text{Fe}_{0.8}\text{O}_3$  (LSCF) was deposited on top of the electrolyte using the cathode ink consisting of LSCF powder, an azeotrope solvent, polyvinyl butyral as a binder and menhaden fish oil as the dispersant. The cathode ink was dip-coated and sintered at  $800\text{ }^\circ\text{C}$  for 3 h.

The cross-sectional SEM images of the cells with the MS and CS electrolyte layers are shown in Figure 18. The CS electrolyte layer is homogeneous, in contrast to the MS one. In the MS electrolyte, the layer facing the Ni-YSZ anode consisted of the almost melted particles of Ni and YSZ sintered together, while the outer side was dense and homogeneous, with a small number of closed pores. It was supposed that the exothermic oxidation of Ni combined

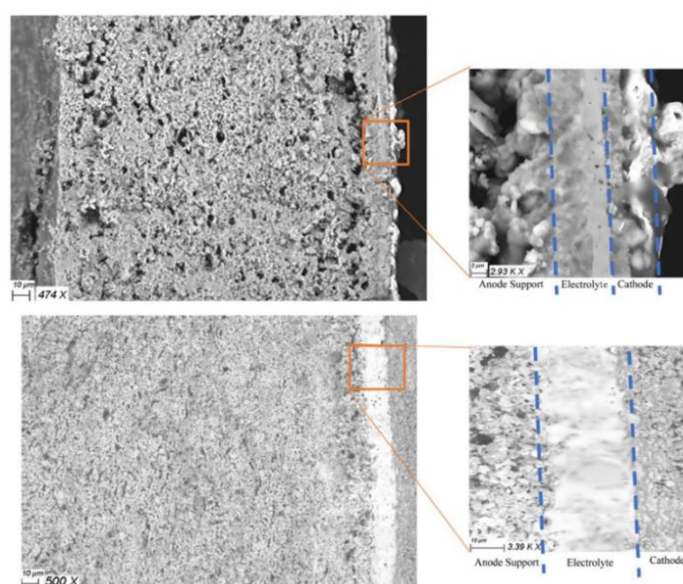


**Figure 18** Cross-sectional SEM images of the cells with the microwave (top) and conventionally (bottom) sintered electrolyte layers [108].

with the microwave irradiation could result in local heating and Ni melting.

The fabricated cells were tested using  $\text{H}_2 + 3 \text{ vol. } \% \text{ H}_2\text{O}$  as a fuel and air as an oxidant. The  $I$ - $V$  and current density curves of the cells are presented in Figure 19. As can be seen, the OCV values of both cells are close to the theoretical values obtained by using the Nernst equation, which proves a good gas-tightness of the electrolyte layer in both cells. As to the power density, at lower temperature, the power performance of both cells is similar, while at high temperatures, the cell with the MS electrolyte is inferior to that with the CS electrolyte.

To explain these peculiarities, the impedance of the cells was measured (see Figure 20). The rightmost semicircles in the impedance spectra with a characteristic frequency of 8 Hz were ascribed to the mass transfer in the electrodes. The concentration polarization of the cell with the microwaved electrolyte was higher compared to the conventionally prepared electrolyte, which explains the worse  $I$ - $V$  performance of the former. It was concluded that MS processing leads to more rapid aggregation and reduces the overall porosity in the supporting anode, making it difficult for the redox active gaseous species to reach the electrolyte. The ohmic part of the impedance related to the electrolyte was less in the case of microwaved sample, which can be due to the better crystallization and densification of the electrolyte. This study showed that MS processing results in the cell electrochemical performance comparable to the conventional sintering techniques except some electrode polarization because of not optimized microstructure of the supporting Ni-YSZ anode.

Hussain et al. [109] reported on the fabrication and testing of a planar large-area anode-supported fuel cell, which was co-sintered using MS technology. NiO-8YSZ composite was used as the supporting anode,  $(\text{Sc}_2\text{O}_3)_{0.10}(\text{CeO}_2)_{0.01}(\text{ZrO}_2)_{0.89}$  (ScCeSZ) and  $\text{Gd}_{0.1}\text{Ce}_{0.9}\text{O}_{1.95}$  (GDC) were used to fabricate the electrolyte and buffer layers, and NiO-ScCeSZ composite was used as the anode functional layer (AFL). All these layers produced by tape-casting were co-laminated by the isostatic pressing at  $70^\circ\text{C}$ . The laminated assembly was laser cut into squares of  $8 \times 8 \text{ cm}^2$  and calcined at  $350^\circ\text{C}$  for 5 h to burn out the organic additives. Then, the half-cells were co-sintered in a microwave furnace at 2.45 GHz and  $1250^\circ\text{C}$  for 20 min, with a heating rate of  $25^\circ\text{C} \cdot \text{min}^{-1}$ . The total duration of the half-cell fabrication using MS process (MS cell) was 90 min. For comparison, similar half-cells were sintered conventionally (CS cell) at the same temperature for 24.5 h, with a heating rate of  $0.5^\circ\text{C} \cdot \text{min}^{-1}$ . The total time of CS, including the heating and cooling processes, was 16 times longer than with MS. In both MS and CS cells,

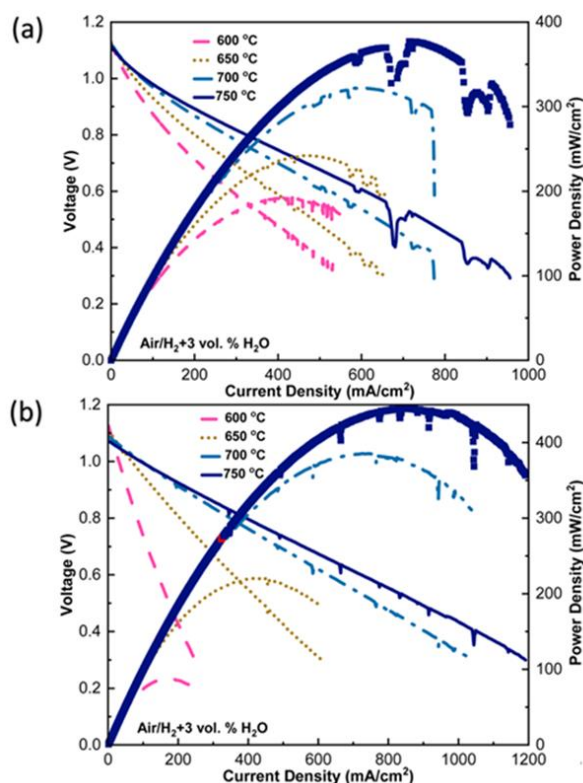


**Figure 19**  $I$ - $V$  and power density curves of single fuel cells with (a) microwave sintered and (b) conventionally sintered 8YSZ electrolyte measured at  $700^\circ\text{C}$  [108].

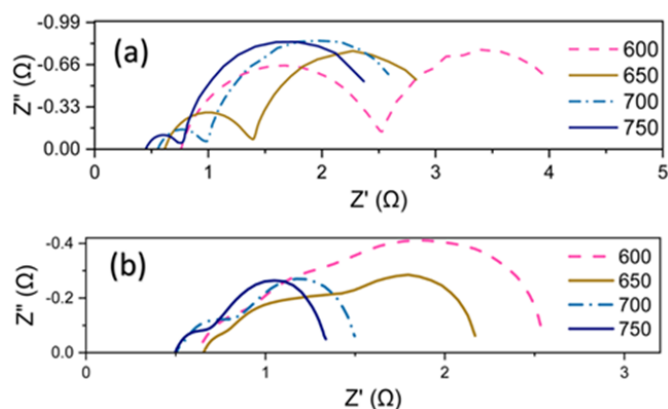


**Figure 20** Nyquist plots (not normalized) of fuel cells with (a) microwave sintered and (b) conventionally sintered 8YSZ electrolyte [108].

the cathode layer was prepared by screen-printing  $\text{La}_{0.6}\text{Sr}_{0.4}\text{CoO}_3$  paste on the free surface of GDC layer of and sintering at  $950^\circ\text{C}$  for 3 h.

SEM study of the cross-sections of MS and CS cells (Figure 21) revealed that the ScCeSZ electrolyte layer was dense and homogenous, with a thickness of  $5\text{--}6 \mu\text{m}$ , in both cells, while the GDC buffer layer with a thickness of  $2\text{--}3 \mu\text{m}$  was denser in the MS cell. Besides, the interfacial porosity between the ScCeSZ and GDC layers was observed in the CS cell, in contrast to the MS cell. Thus, the MS processing resulted in better adhesion and denser microstructure than the CS route.

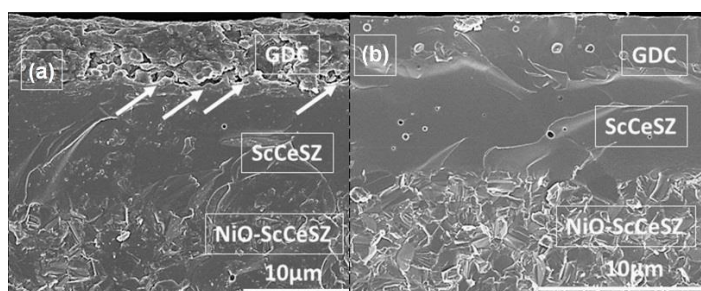


**Figure 21** SEM images of the conventionally (a) and microwave (b) sintered cells [109].

The electrochemical testing revealed that the both cells demonstrated a high open circuit voltage (OCV) of  $\sim 1.1$  V at  $700\text{--}750$  °C, when hydrogen was used as a fuel and air as an oxidant, which confirmed the excellent gas-tightness of the electrolyte layer observed in the SEM micrographs. The peak power density (PPD) of the MS cell was  $0.7$  and  $1.05$   $\text{W} \cdot \text{cm}^{-2}$  at  $700$  and  $750$  °C, respectively, while the PPD of the CS cell was  $0.41$  and  $0.67$   $\text{W} \cdot \text{cm}^{-2}$  at  $700$  and  $750$  °C, respectively. So, the CS cell exhibited a lower power output compared to the MS cell. To find out the reasons for such electrochemical behavior, the impedance of the cells was studied. It was found that the electrolyte resistance in the MS cell was lower than in CS cell ( $0.15$  and  $0.26$   $\Omega \cdot \text{cm}^2$  at  $750$  °C, respectively), which can be explained by better densification during MS processing. In contrast, the electrode polarization resistance of the MS cell was higher compared to the CS cell, that could be caused by the sluggish gas transport through the less porous anode support. Therefore, further optimization of the microstructure of the MS anode support is required. These results are consistent with those obtained by Amiri et al. [108] discussed above.

Wang et al. [47] fabricated the proton-conducting SOFC with  $\text{BaZr}_{0.1}\text{Ce}_{0.66}\text{Ni}_{0.04}\text{Y}_{0.2}\text{O}_{3-\delta}$  (BZCNY) electrolyte thin layer on the supporting NiO-based anode by the one step MS processing. NiO-BZCNY composite anode powder was pressed into a disk at  $100$  MPa. Then, the BCZY film was fabricated by pressing the electrolyte powder onto the NiO-BZCNY disk under a pressure of  $150$  MPa. The composite cathode layer was prepared by painting the free electrolyte surface with the slurry containing the powders of  $\text{Sm}_{0.5}\text{Sr}_{0.5}\text{CoO}_{3-\delta}$  (SSC) and BCZY. The green three-layer NiO-BZCNY/BZCNY/SSC-BCZY cell was co-sintered in a microwave furnace at  $1100$  °C for  $2$  h. For comparison, the identical cell was co-sintered conventionally (CS) at  $1100$  °C for  $2$  h in a traditional electrical furnace.

SEM images of the cross-sections of the MS and CS cells are presented in Figure 22. As can be seen, the MS processing improved the densification of the electrolyte,

as well as the interfacial contacts with electrodes while maintaining the porous structure of the electrodes. Such microstructures of the functional layers are beneficial for the SOFC efficiency.

The performance of the fuel cells was tested using wet  $\text{H}_2$  as a fuel and static air as an oxidant (Figure 23). The MS cell exhibited a significantly higher power density than the CS cell ( $\sim 450$   $\text{mW} \cdot \text{cm}^{-2}$  vs  $\sim 300$   $\text{mW} \cdot \text{cm}^{-2}$  at  $700$  °C) and higher current densities.

The MS sintering of dense proton-conducting  $\text{BaCe}_{0.7}\text{Zr}_{0.1}\text{Y}_{0.2}\text{O}_{3-\delta}$  (BCZY) electrolyte was described in [46]. The precursor nanopowder of  $\text{BaCe}_{0.7}\text{Zr}_{0.1}\text{Y}_{0.2}\text{O}_{3-\delta}$  was synthesized by the combustion method. The BCZY electrolyte layer was deposited on the composite NiO-BCZY anode substrate by the co-pressing method. The obtained green bi-layer tapes were co-sintered in a microwave furnace at  $1200$  °C for  $2$  h.

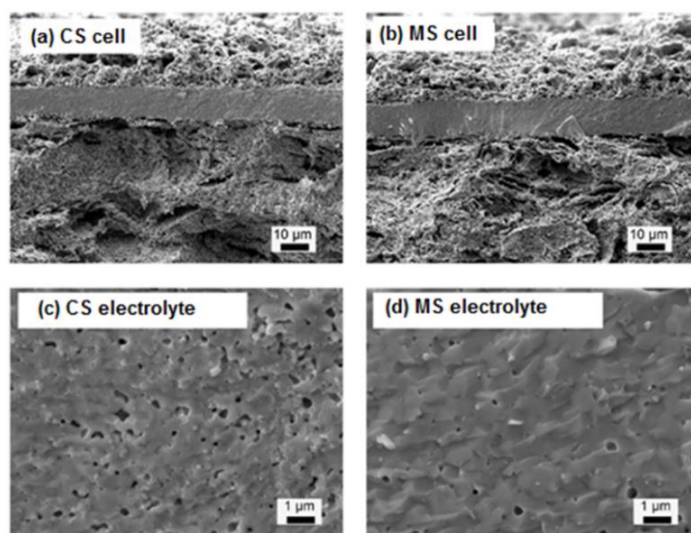


**Figure 22** Cross-sectional SEM images of one-step co-sintered NiO-BZCNY/BZCNY/SSC-BCZY cells sintered in the conventional furnace (a, c) and in the microwave furnace (b, d) [47].

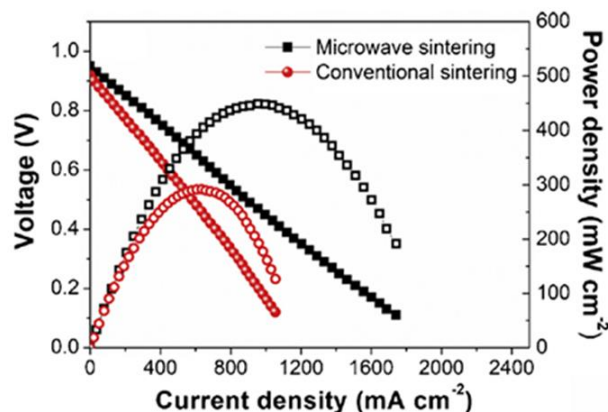


**Figure 23** (a)  $I$ - $V$  and power density curves measured at  $700$  °C for one-step co-sintered cells sintered in the conventional furnace and in the microwave furnace [47].

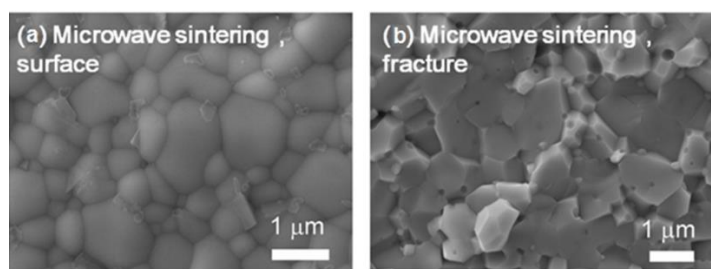


**Figure 24** SEM micrographs of microwave sintered BCZY ceramics after the thermal treatment at 1200 °C for 2 h: (a) surface, (b) fracture [46].

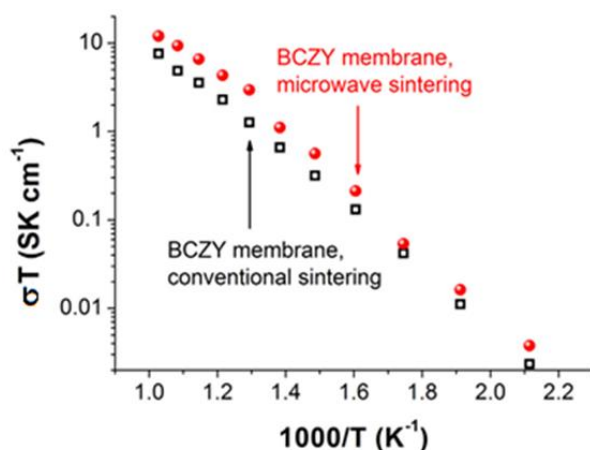


**Figure 25** Electrical conductivity of  $\text{BaCe}_{0.7}\text{Zr}_{0.1}\text{Y}_{0.2}\text{O}_{3-\delta}$  ceramics densified by microwave and conventional sintering [46].

SEM study of the MS processed BCZY layer, revealed its dense morphology with grains of 0.3–1.0  $\mu\text{m}$  (Figure 24). The conductivity investigation of the MS processed and conventionally sintered (at 1400 °C) BCZY samples by the impedance spectroscopy showed that the MS sample had a higher conductivity than BCZY densified using CS (Figure 25).

As was discussed above, the conventional sintering of refractory proton-conducting oxides, which is conducted at high temperatures with long expositions, is fraught with loss of volatile elements, especially barium, which results in the degradation of electrical conductivity. Zhong et al. [110] showed that the MS-processed (1400 °C, 2 h)  $\text{BaZr}_{0.1}\text{Ce}_{0.7}\text{Y}_{0.1}\text{Yb}_{0.1}\text{O}_{3-\delta}$  (BZCYYb) electrolyte with a relative density as high as 97.6 % had the barium content close to the nominal one (50.77 at. %), in contrast to the sample that was sintered conventionally (at 1550 °C) and had only 36.66 at. % Ba. So, decreasing temperature for 150 °C resulted in the suppression of Ba evaporation. Due to the maintained composition and coarse-grained microstructure, the MS-processed BZCYYb ceramic demonstrated the conductivity as high as 38  $\text{mS} \cdot \text{cm}^{-1}$  at 700 °C in wet air.

Thus, available literature data prove that the MS technology is effective for obtaining dense ion-conducting ceramics. Fast processing and low sintering temperatures allows to avoid the evaporation of volatile elements. Due to the high density and stoichiometric composition, MS electrolytes demonstrate enhanced functional properties. MS is a promising technology for fabrication of large-area planar cells as well as tubular cells, at a lower temperature and a shorter time than with conventional sintering.

## 5. Comparison between Sintering Technologies

Table 1 summarizes the sintering technologies, sintering regimes, microstructural characteristics and electrical conductivities of ion-conducting ceramics. The presented results demonstrate the key advantages of FASTs to lower the sintering temperature and reduce the duration of sintering process compared to the conventional sintering. As follows from the table, using FASTs it is possible to obtain ceramics with grain sizes from tens of nanometers to several micrometers, which allows tuning the functional properties sensitive to the microstructure. The results on the transport properties of the FAST-processed ion-conducting ceramics reported in the literature show that the field-assisted technologies can significantly alter the electrical conductivity, which must be taken into account. The technology impact can be both positive and negative, depending on the microstructure of resulting ceramics.

## 6. Conclusions

In the present article, the applications of FASTs for densification of refractory oxygen-ion and proton conducting ceramics are reviewed. The mechanisms, advantages and limitations of FASTs are examined, and the impact of sintering technology on the microstructural and transport properties of electrolyte materials, and the performance of FAST-processed electrochemical cells is discussed.

Analysis of the results on FAST processing of solid oxide electrolytes reported in literature shows that these methods can be effectively used to fabricate high-density ion-conducting ceramics, which are required for the use as membranes in the solid oxide electrochemical devices. The key advantage of FASTs is the ability to consolidate material in a short time at a relatively low temperature. Due to these benefits, these technologies are used to obtain nanocrystalline ceramic and composite materials with specific properties. At the same time, different microstructures can be obtained by varying the sintering parameters of FASTs, including coarse-grained ceramics. Another benefit of FASTs is the minimized loss of volatile components, in contrast to conventional sintering, due to

the low temperature and short duration of processing. However, despite these advantages, the field-assisted technologies can significantly alter the electrical properties of ion-conducting ceramics. Nonetheless, when optimizing the parameters of the sintering process, FASTs

make it possible to obtain materials with a required composition, morphology and functional properties faster and more economically efficient compared to traditional technologies.

**Table 1** – Sintering technologies, sintering regimes, microstructural characteristics and electrical conductivity of ion-conducting ceramics (CS – conventional sintering, SPS – spark plasma sintering, MS – microwave sintering, FS – flash sintering).

Composition	Sintering technology, heating rate, temperature of sintering, dwell time, atmosphere	Relative density (% theoretical density)	Grain size	Electrical conductivity	Ref
8YSZ	CS 1700 °C, 12 h	N/A	18 μm	0.14 mS · cm <sup>-1</sup> at 420 °C 4 mS · cm <sup>-1</sup> at 600 °C	[96]
8YSZ	CS 1500 °C, 2 h 1525 °C, 2 h 1550 °C, 2 h	98.5 99.4 99.5	4.12 μm 4.67 μm 8.83 μm	N/A	[72]
8YSZ	SPS 100 °C · min <sup>-1</sup> , 5 min, 50 MPa 1250 °C 1325 °C	99.1 99.5	1.30 μm 1.16 μm	N/A	[72]
8YSZ	MS 10 °C · min <sup>-1</sup> , 15 min 1500 °C 1525 °C 1550 °C	98.6 99.2 99.2	2.77 μm 3.70 μm 5.22 μm	N/A	[72]
8YSZ	FS 53.3 V · cm <sup>-1</sup> , 1000 Hz 964 °C	94	200 nm	0.17 mS · cm <sup>-1</sup> at 420 °C in air	[95]
8YSZ	FS 10 °C · min <sup>-1</sup> , 50 V · cm <sup>-1</sup> 1070 °C	95.7	1–3 μm	6 mS · cm <sup>-1</sup> at 600 °C in air	[89]
8YSZ	FS 75 V · cm <sup>-1</sup> 825 °C, air 745 °C, Ar 730 °C, Ar/H <sub>2</sub>	95 – 68	0.5–3 μm	N/A	[98]
8YSZ	FS 10 °C · min <sup>-1</sup> , 0–500 V cm <sup>-1</sup> 800–975 °C	48–90 at 0.3–3 A cm <sup>-2</sup> 92–97 at 6 A cm <sup>-2</sup>	100 nm 200 nm	N/A	[87]
BaZrO <sub>3</sub>	SPS 200 °C · min <sup>-1</sup> , 1 min, 105 MPa 1400 °C 1600 °C	91.3 98.5	70–150 nm 200 nm	N/A	[75]
BaZr <sub>0.9</sub> Y <sub>0.1</sub> O <sub>3-d</sub>	SPS	99	500 nm	65 mS · cm <sup>-1</sup>	[76]

	150 °C · min <sup>-1</sup> , 5 min, 100 MPa 1600–1700 °C SPS			at 800 °C in wet O <sub>2</sub> ( <i>p</i> H <sub>2</sub> O = 0.015 atm)	
BaZr <sub>1-x</sub> Ho <sub>x</sub> O <sub>3-d</sub>				49 mS · cm <sup>-1</sup>	[44]
<i>x</i> = 0.1	1600 °C, 75 MPa, 20 min	99.5	0.6–1 μm	at 700 °C in wet O <sub>2</sub> ( <i>p</i> H <sub>2</sub> O = 0.03 atm)	
<i>x</i> = 0.2		99.1	0.2–0.6 μm		
BaZr <sub>0.9</sub> Y <sub>0.1</sub> O <sub>3-d</sub>	SPS	94	90 nm	0.06 mS · cm <sup>-1</sup>	[78]
	200 °C · min <sup>-1</sup> , 5 min, 100 MPa 1400 °C			at 400 °C in wet air ( <i>p</i> H <sub>2</sub> O = 0.023 atm)	
BaZr <sub>0.9</sub> Y <sub>0.1</sub> O <sub>3-d</sub>	SPS				[43]
	4 MPa, 5 min 1200 °C	low density	< 200 nm		
	1300 °C	85.5	200 nm	0.02 mS · cm <sup>-1</sup>	
	1400 °C	92.4	260 nm	0.03 mS · cm <sup>-1</sup>	
BaZr <sub>0.7</sub> Ce <sub>0.2</sub> Y <sub>0.1</sub> O <sub>3-d</sub>	SPS	99.7	300–600 nm	at 700 °C in wet air ( <i>p</i> H <sub>2</sub> O = 0.03 atm)	[79]
	150 °C · min <sup>-1</sup> , 5 min, 80 MPa 1550 °C			at 600 °C in 5 % H <sub>2</sub> /Ar ( <i>p</i> H <sub>2</sub> O = 0.03 atm)	
BaCe <sub>0.9-x</sub> Zr <sub>x</sub> Y <sub>0.1</sub> O <sub>3-d</sub>	SPS	70 at <i>x</i> = 0	150 nm at	<i>x</i> = 0.5:	[80]
<i>x</i> = 0, 0.5–0.8	57 MPa, 5 min 900 °C	60 at <i>x</i> > 0	<i>x</i> = 0	0.3 mS · cm <sup>-1</sup>	
			80 nm at	at 550 °C in air	
			<i>x</i> = 0.5		
BaZr <sub>0.92</sub> Y <sub>0.08</sub> O <sub>3-d</sub>	SPS	> 98	85 nm	0.001 mS · cm <sup>-1</sup>	[77]
	200 °C · min <sup>-1</sup> , 100 MPa, 5 min 1400–1500 °C			at 300 °C in wet N <sub>2</sub> ( <i>p</i> H <sub>2</sub> O = 0.023 atm)	
BaCe <sub>0.8</sub> Gd <sub>0.2</sub> O <sub>3-d</sub>	FS	84	2–3 μm	N/A	[91]
	0–140 V · cm <sup>-1</sup> , 1000 Hz 910 °C				
BaZr <sub>0.1</sub> Ce <sub>0.7</sub> Y <sub>0.1</sub> Yb <sub>0.1</sub> O <sub>3-d</sub>	FS	N/A	0.9 μm at	30 mS · cm <sup>-1</sup>	[40]
	10 °C · min <sup>-1</sup> to 850 °C 60–80 V · cm <sup>-1</sup>		9 A · cm <sup>-2</sup>	at 700 °C in wet H <sub>2</sub> ( <i>p</i> H <sub>2</sub> O = 0.03 atm)	
BaZr <sub>0.1</sub> Ce <sub>0.7</sub> Y <sub>0.2</sub> O <sub>3-d</sub> + + 0.5 wt % NiO	FS	N/A	5.5 μm	14 mS · cm <sup>-1</sup>	[41]
	10 °C · min <sup>-1</sup> , 200 V · cm <sup>-1</sup>			at 700 °C in air	
BaCe <sub>0.7</sub> Zr <sub>0.1</sub> Y <sub>0.2</sub> O <sub>3-d</sub>	MS	N/A	0.3–1 μm	10 mS · cm <sup>-1</sup>	[46]
	1200 °C, 2 h			at 700 °C, wet H <sub>2</sub> /air	

## Supplementary materials

No supplementary materials are available.

## Funding

This research had no external funding.

## Acknowledgments

None.

## Author contributions

Liliya A. Dunyushkina: Conceptualization; Writing – Original draft; Data curation; Formal Analysis; Writing – Review & Editing.

## Conflict of interest

The authors declare no conflict of interest.

## Additional information



Liliya Dunyushkina (Dr.Sc.) graduated from Department of Physics of the Ural State University named by M. Gorky (Sverdlovsk, USSR) in 1990. She earned her PhD degree in Physical Chemistry from the same university in 1995. Since 2017, she has held a Doctor of Science degree at the Institute of High Temperature Electrochemistry. She has been

working as a senior and leading researcher at the Institute of High Temperature Electrochemistry since 1995. Research Interests: transport properties of ionic systems, dynamics of interface processes, electrochemical generation of energy, optimization of electrolyte and electrode materials, chemical solution deposition of solid-oxide films.

## References

- He S, Zou Y, Chen K, Jiang SP, A critical review of key materials and issues in solid oxide cells, *Interdisciplinary Materials*, **2(1)** (2023) 111–136. <https://doi.org/10.1002/idm2.12068>
- Wolf SE, Winterhalder FE, Vibhu V, de Haart LGJ (Bert), et al., Solid oxide electrolysis cells – current material development and industrial application, *J. Mater. Chem. A*, **11** (2023) 17977–18028. <https://doi.org/10.1039/D3TA02161K>
- Etsell TH, Flengas SN, Electrical properties of solid oxide electrolytes, *Chem. Rev.*, **70(3)** (1970) 339–376. <https://doi.org/10.1021/cr60265a003>
- Kreuer KD, Proton-conducting oxides, *Annu. Rev. Mater. Res.*, **33** (2003) 333–359. <https://doi.org/10.1146/annurev.matsci.33.022802.091825>
- Hossain S, Abdalla AM, Jamain SNB, Zaini JH, et al., A review on proton conducting electrolytes for clean energy and intermediate temperature-solid oxide fuel cells, *Renew. Sustain. Energy Rev.*, **79** (2017) 750–764. <https://doi.org/10.1016/j.rser.2017.05.147>
- Duan C, Huang J, Sullivan N, O'Hayre R, Proton-conducting oxides for energy conversion and storage, *Appl. Phys. Rev.*, **7** (2020) 011314. <https://doi.org/10.1063/1.5135319>
- Choi S, Davenport TC, Haile SM, Protonic ceramic electrochemical cells for hydrogen production and electricity generation: exceptional reversibility, stability, and demonstrated faradaic efficiency, *Energy Environ. Sci.*, **12** (2019) 206–215. <https://doi.org/10.1039/C8EE02865F>
- Yatoo MA, Habib F, Malik AH, Qazi MJ, et al., Solid-oxide fuel cells: A critical review of materials for cell components, *MRS Communications*, **13** (2023) 378–384. <https://doi.org/10.1557/s43579-023-00371-0>
- Yin S, Li M, Zeng Y, Li C, et al., Study of  $\text{Sm}_{0.2}\text{Ce}_{0.8}\text{O}_{1.9}$  (SDC) electrolyte prepared by a simple modified solid-state method, *Journal of Rare Earths*, **32(8)** (2014) 767–771. [https://doi.org/10.1016/S1002-0721\(14\)60138-1](https://doi.org/10.1016/S1002-0721(14)60138-1)
- Chourashiya MG, Patil JY, Pawar SH, Jadhav LD, Studies on structural, morphological and electrical properties of  $\text{Ce}_{1-x}\text{Gd}_x\text{O}_{2-(x/2)}$ , *Materials Chemistry and Physics*, **109(1)** (2008) 39–44. <https://doi.org/10.1016/i.matchemphys.2007.10.028>
- Matsui K, Yoshida H, Ikuhara Y, Grain-boundary structure and microstructure development mechanism in 2–8 mol % yttria-stabilized zirconia polycrystals, *Acta Materialia*, **56(6)** (2008) 1315–1325. <https://doi.org/10.1016/j.actamat.2007.11.026>
- Kim B-N, Suzuki TS, Morita K, Yoshida H, et al., Densification kinetics during isothermal sintering of 8YSZ, *J. Eur. Ceram. Soc.*, **36(5)** (2016) 1269–1275. <https://doi.org/10.1016/j.jeurceramsoc.2015.11.041>
- Han M, Tang X, Peng S, Research on sintering process of YSZ electrolyte, *Rare Metals*, **25(6)** (2006) 209–212. [https://doi.org/10.1016/S1001-0521\(08\)60083-2](https://doi.org/10.1016/S1001-0521(08)60083-2)
- Azad A, Subramaniam S, Dung TW, On the development of high density barium metazirconate ( $\text{BaZrO}_3$ ) ceramics, *J. Alloys Compd.*, **334** (2002) 118–30. [https://doi.org/10.1016/S0925-8388\(01\)01785-6](https://doi.org/10.1016/S0925-8388(01)01785-6)
- Yamazaki Y, Hernandez-Sanchez R, Haile SM, High total proton conductivity in large-grained yttrium-doped barium zirconate, *Chem. Mater.*, **21** (2009) 2755–2762. <https://doi.org/10.1021/cm900208w>
- Gorelov VP, Balakireva VB, Kleshchev YN, et al., Preparation and electrical conductivity of  $\text{BaZr}_{1-x}\text{R}_x\text{O}_{3-a}$  ( $\text{R} = \text{Sc}, \text{Y}, \text{Ho}, \text{Dy}, \text{Gd}, \text{In}$ ), *Inorg. Mater.*, **37(5)** (2001) 535–538. <https://doi.org/10.1023/A:1017553506634>
- Han D, Hatada N, Uda T, Microstructure, proton concentration and proton conductivity of barium zirconate doped with Ho, Er, Tm and Yb, *J. Electrochem. Soc.*, **163(6)** (2016) F470–F476. <https://doi.org/10.1149/2.0551606jes>
- Park GS, Mo SI, Kim JH, et al., Characteristics of  $\text{Li}_2\text{CO}_3$  as sintering aid for  $\text{Ce}_{0.8}\text{Sm}_{0.2}\text{O}_{2-\delta}$  electrolyte in solid oxide fuel cells, *Korean J. Chem. Eng.*, **39** (2022) 1796–1804. <https://doi.org/10.1007/s11814-022-1112-5>
- Mirzaei A, Afzali M, Khachatourian AM, Golmohammad M, Enhancing sintering behavior and conductivity of YSZ electrolyte by co-doping of ZnO and  $\text{MnO}_2$ , *Materials Chemistry and Physics*, **315** (2024) 129051. <https://doi.org/10.1016/j.matchemphys.2024.129051>
- Babilo P, Haile SM, Enhanced sintering of yttrium-doped barium zirconate by addition of ZnO, *J. Am. Ceram. Soc.*, **88(9)** (2005) 2362–2368. <https://doi.org/10.1111/j.1551-2916.2005.00449.x>
- Qiao Z, Li S, Li Y, Wu Q, et al., Sintering behavior and physical properties of ZnO-modified  $\text{BaZrO}_3$  ceramics, *Int. J. Appl. Ceram. Technol.*, **21** (2024) 124–132. <https://doi.org/10.1111/ijac.14500>
- Huang Y, Merkle R, Maier J, Effects of NiO addition on sintering and proton uptake of  $\text{Ba}(\text{Zr,Ce,Y})\text{O}_{3-\delta}$ , *J. Mater. Chem. A*, **9** (2021) 14775. <https://doi.org/10.1039/D1TA02555D>
- Han D, Uemura S, Hiraiwa C, Majima M, et al., Detrimental effect of sintering additives on conducting ceramics: yttrium-doped barium zirconate, *ChemSusChem*, **11** (2018) 4102–4113. <https://doi.org/10.1002/cssc.201801837>
- Porfirio TC, Muccillo ENS, Muccillo R, Electric field-assisted synthesis/sintering cerium oxide: 5 wt. % gadolinium

- oxide, *J. Eur. Ceram. Soc.*, **41(14)** (2021) 7105–7110, <https://doi.org/10.1016/j.jeurceramsoc.2021.07.027>
25. Xu J, Liu Z, Xie Z, He S, et al., DC electric field-assisted hot pressing of zirconia: Methodology, phenomenology, and sintering mechanism, *J. Am. Ceram. Soc.*, **104** (2021) 5571–5583. <https://doi.org/10.1111/jace.17963>
26. Guillon O, Gonzalez-Julian J, Dargatz B, Kessel T, et al., Field-assisted sintering technology/spark plasma sintering: mechanisms, materials, and technology developments, *Adv. Eng. Mater.*, **16** (2014) 830–849. <https://doi.org/10.1002/adem.201300409>
27. Manière C, Harnois C, Riquet G, Lecourt J, et al., Flash spark plasma sintering of zirconia nanoparticles: Electro-thermal-mechanical-microstructural simulation and scalability solutions. *J. Eur. Ceram. Soc.*, **42(1)** 2022 216–226. <https://doi.org/10.1016/j.jeurceramsoc.2021.09.021>
28. Raj R, Joule heating during flash-sintering, *J. Eur. Ceram. Soc.*, **32** (2012) 2293–2301. <https://doi.org/10.1016/j.jeurceramsoc.2012.02.030>
29. Raj R, Cologna M, Francis JSC, Influence of externally imposed and internally generated electrical fields on grain growth, diffusional creep, sintering and related phenomena in ceramics, *J. Am. Ceram. Soc.*, **94** (2011) 1941–65. <https://doi.org/10.1111/j.1551-2916.2011.04652.x>
30. Naik K, Sglavo VM, Raj R, Flash sintering as a nucleation phenomenon and a model thereof, *J. Eur. Ceram. Soc.*, **34** (2014) 4063–4067. <https://doi.org/10.1016/j.jeurceramsoc.2014.04.043>
31. Wu J, Wu X, Gao Y, Yan Z, Innovations in electric current-assisted sintering for SOFC: a review of advances in flash sintering and ultrafast high-temperature sintering, *Appl. Sci.*, **14** (2024) 3953. <https://doi.org/10.3390/app14103953>
32. Aman B, Acharya S, Reeja-Jayan B, Making the case for scaling up microwave sintering of ceramics, *Adv. Eng. Mater.*, **26** (2024) 2302065. <https://doi.org/10.1002/adem.202302065>
33. Agrawal DK, Microwave processing of ceramics: a review, *Current Opinion in Solid State & Mat. Sci.*, **3(5)** (1998) 480–486. [https://doi.org/10.1016/S1359-0286\(98\)80011-9](https://doi.org/10.1016/S1359-0286(98)80011-9)
34. Binner JGP, Vaidhyanathan B. Microwave sintering of ceramics: what does it offer? *Key Eng. Mat.*, **264–268** (2004) 725–730. <https://doi.org/10.4028/www.scientific.net/KEM.264-268.725>
35. Fu M, Lin X, Li X, Tao Z, Applications of microwave technology in the field of solid oxide fuel cell – a review, *Russ. Chem. Rev.*, **92(9)** (2023) RCR5092. <https://doi.org/10.59761/RCR5092>
36. Agrawal D. Microwave sintering of ceramics, composites and metal powders, Editor(s): Zhigang Zak Fang, In *Woodhead Publishing Series in Metals and Surface Engineering, Sintering of Advanced Materials*, Woodhead Publishing, 2010, Pages 222–248, ISBN 9781845695620
37. Oghbaei M, Mirzaee O, Microwave versus conventional sintering: a review of fundamentals, advantages and applications, *J. Alloys Compd.*, **494(1–2)** (2010) 175–189. <https://doi.org/10.1016/j.jallcom.2010.01.068>
38. Chiu WT, Chen CL, Chen YY, A strategy to optimize the thermoelectric performance in a spark plasma sintering process, *Sci. Rep.*, **6** (2016) 23143. <https://doi.org/10.1038/srep23143>
39. Prette ALG, Cologna M, Sglavo V, Raj R, Flash-sintering of  $\text{Co}_2\text{MnO}_4$  spinel for solid oxide fuel cell applications, *J. Power Sources*, **196** (2011) 2061–2065. <https://doi.org/10.1016/j.jpowsour.2010.10.036>
40. Jiang T, Liu Y, Wang Z, Sun W, et al., An improved direct current sintering technique for proton conductor -  $\text{BaZr}_{0.1}\text{Ce}_{0.7}\text{Y}_{0.1}\text{Yb}_{0.1}\text{O}_3$ : the effect of direct current on sintering process, *J. Power Sources*, **248** (2014) 70–76. <http://dx.doi.org/10.1016/j.jpowsour.2013.09.042>
41. Soleimany M, Paydar MH, Wang S, Enhancing the flash-sinterability of  $\text{BaZr}_{0.1}\text{Ce}_{0.7}\text{Y}_{0.2}\text{O}_{3-d}$  proton-conducting electrolyte by nickel oxide doping for possible application in SOFCs, *Int. J. Hydrogen En.*, **46(19)** (2021) 11115–11126. <https://doi.org/10.1016/j.ijhydene.2020.06.112>
42. Han M, Tang X, Yin H, Peng S, Fabrication, microstructure and properties of a YSZ electrolyte for SOFCs, *J. Power Sources*, **16(2)** (2007) 757–763. <https://doi.org/10.1016/j.jpowsour.2006.11.054>
43. Wang S, Liu Y, He J, Chen F, et al., Spark-plasma-sintered barium zirconate based proton conductors for solid oxide fuel cell and hydrogen separation applications, *Int. J. Hydrogen Energy*, **40** (2015) 5707–5714. <https://doi.org/10.1016/j.ijhydene.2015.02.116>
44. Saini DS, Ghosh A, Tripathy S, Sharma SK, et al., Improved conductivity of spark plasma sintered Ho-substituted  $\text{BaZrO}_3$  electrolyte ceramics for IT-SOFCs, *ACS Appl. Energy Mater.*, **1** (2018) 3469–3478. <https://doi.org/10.1021/acsaem.8b00655>
45. Ahmed I, Kinyanjui FG, Steegstra P, Shen ZJ, et al., Improved proton conductivity in spark-plasma sintered dense ceramic  $\text{BaZr}_{0.5}\text{In}_{0.5}\text{O}_{3-\delta}$ , *Electrochemical and Solid-State Letters*, **13(11)** (2010) B130–B134. <https://doi.org/10.1149/1.3482016>
46. Xu X, Bi L, Zhao XS, Highly-conductive proton-conducting electrolyte membranes with a low sintering temperature for solid oxide fuel cells, *J. Membr. Sci.*, **558** (2018) 17–25. <https://doi.org/10.1016/j.memsci.2018.04.037>
47. Wang B, Bi L, Zhao XS, Fabrication of one-step co-fired proton-conducting solid oxide fuel cells with the assistance of microwave sintering, *J. Eur. Ceram. Soc.*, **38(16)** (2018) 5620–5624. <https://doi.org/10.1016/j.jeurceramsoc.2018.08.020>
48. Khoshghadam-Pireyousefan M, Mohammadzadeh A, Heidarzadeh A, Brabazon D, Fundamentals of spark plasma sintering for metallic, ceramic, and polymer matrix composites production, Editor(s): Dermot Brabazon, *Encyclopedia of Materials: Composites*, Elsevier, 2021, Pages 822–836, ISBN 9780128197318. <https://doi.org/10.1016/B978-0-12-803581-8.11907-1>
49. Tokita M. Spark Plasma Sintering (SPS) method, systems, and applications, in *Handbook of Advanced Ceramics*, 2nd Ed. (2013), Chapter 11.2.3, 1149–1177.
50. Bram M, Laptev AM, Mishra TP, Nur K, et al., Application of Electric Current-Assisted Sintering Techniques for the Processing of Advanced Materials, *Adv. Eng. Mater.*, **22** (2020) 2000051. <https://doi.org/10.1002/adem.202000051>
51. Supriya S, Electric field assisted spark plasma sintering of ABO<sub>3</sub> perovskites: Crystal structure, dielectric behavior and future challenges, *Open Ceramics*, **18** (2024) 100608. <https://doi.org/10.1016/j.oceram.2024.100608>
52. Harrison RW, Morgan J, Buckley J, Bostanchi S, et al., Development and comparison of field assisted sintering

- techniques to densify CeO<sub>2</sub> ceramics, *J. Eur. Ceram. Soc.*, **42**(14) (2022) 6599–6607. <https://doi.org/10.1016/j.jeurceramsoc.2022.06.079>
53. Kandi H, Koona R, Raju GMJ, Synthesis of SrHfO<sub>3</sub> co-doped with Gd<sub>2</sub>O<sub>3</sub> and Yb<sub>2</sub>O<sub>3</sub> for thermal barrier coating applications, *Materials Today: Proceedings*, **47**(9) (2021) 1904–1907. <https://doi.org/10.1016/j.matpr.2021.03.66>
54. Saheb N, Hayat U, Hassan SF, Recent advances and future prospects in Spark Plasma Sintered alumina hybrid nanocomposites, *Nanomaterials*, **9**(11) (2019) 1607. <https://doi.org/10.3390/nano9111607>
55. Alvarez-Clemares I, Mata-Osoro G, Fernández A, Lopez-Esteban S, et al., Transparent alumina/ceria nanocomposites by spark plasma sintering, *Advanced Engineering Materials*, **12**(11) (2010) 1154–1160. <https://doi.org/10.1002/adem.201000176>
56. Yang W, Wang L, Lia Y, Zhou H, et al., An easily sintered, chemically stable indium and tin co-doped barium hafnate electrolyte for hydrogen separation, *J. Alloy. Compd.*, **868** (2021) 159117. <https://doi.org/10.1016/j.jallcom.2021.159117>
57. Belyakov SA, Lesnichyova AS, Balakireva VB, Tarutin AP, et al., ZnO sintering additive without negative impact on proton-conducting SrHf<sub>0.8</sub>Sc<sub>0.2</sub>O<sub>3-δ</sub> electrolyte, *Ceram. Int.* Article in press, <https://doi.org/10.1016/j.ceramint.2024.04.331>
58. Gorelov VP, Balakireva VB, Kleshchev YN, Brusentsov VP, Preparation and electrical conductivity of BaZr<sub>1-x</sub>R<sub>x</sub>O<sub>3-a</sub> (R = Sc, Y, Ho, Dy, Gd, In), *Inorg. Mater.*, **37**(5) (2001) 535–538. <https://doi.org/10.1023/A:1017553506634>
59. Yamazaki Y, Hernandez-Sanchez R, Haile SM, High total proton conductivity in large-grained yttrium-doped barium zirconate, *Chem. Mater.*, **21** (2009) 2755–2762. <https://doi.org/10.1021/cm900208w>
60. Han D, Hatada N, Uda T, Microstructure, proton concentration and proton conductivity of barium zirconate doped with Ho, Er, Tm and Yb, *J. Electrochem. Soc.*, **163**(6) (2016) F470–F476. <https://doi.org/10.1149/2.0551606jes>
61. Gonçalves MD, Maram PS, Navrotsky A, Muccillo R, Effect of synthesis atmosphere on the proton conductivity of Y-doped barium zirconate solid electrolytes, *Ceram. Int.*, **42** (2016) 13689–13696. <https://www.elsevier.com/open-access/userlicense/1.0/>
62. Huang Y, Merkle R, Maier J, Effects of NiO addition on sintering and proton uptake of Ba(Zr,Ce,Y)O<sub>3-δ</sub>, *J. Mater. Chem. A*, **9** (2021) 14775. <https://doi.org/10.1039/D1TA02555D>
63. Han D, Uemura S, Hiraiwa C, Majima M, et al., Detrimental effect of sintering additives on conducting ceramics: yttrium-doped barium zirconate, *ChemSusChem*, **11** (2018) 4102–4113. <https://doi.org/10.1002/cssc.201801837>
64. Han D, Goto K, Hiraiwa C, Majima M, et al., Proton conductive BaZr<sub>0.8-x</sub>Ce<sub>x</sub>Y<sub>0.2</sub>O<sub>3-δ</sub>: influence of NiO sintering additive on crystal structure, hydration behavior, and conduction properties, *ChemSusChem*, **14** (2021) 614–623. <https://doi.org/10.1002/cssc.202002369>
65. Shakel Z, Loureiro FJA, Antunes I, Mikhalev SM, et al., Tailoring the properties of dense yttrium-doped barium zirconate ceramics with nickel oxide additives by manipulation of the sintering profile, *Int. J. Energy Res.*, **46**(15) (2022) 21989–22000. <https://doi.org/10.1002/er.8389>
66. Yang W, Liu Y, Wang L, Zhou H, et al., Investigation on properties of BaZr<sub>0.6</sub>Hf<sub>0.2</sub>Y<sub>0.2</sub>O<sub>3-δ</sub> with sintering aids (ZnO, NiO, Li<sub>2</sub>O) and its application for hydrogen permeation, *Int. J. Hydrogen Energy*, **47**(86) (2022) 36566–36581. <https://doi.org/10.1016/j.ijhydene.2022.08.227>
67. Huang Y, Merkle R, Zhou D, Sigle W, et al., Effect of Ni on electrical properties of Ba(Zr,Ce,Y)O<sub>3-δ</sub> as electrolyte for protonic ceramic fuel cells, *Solid State Ion.*, **390** (2023) 116113. <https://doi.org/10.1016/j.ssi.2022.116113>
68. Trivino-Pelaez A, Perez-Coll D, Aparicio M, Fagg DP, et al., Processing and characterisation of BaZr<sub>0.8</sub>Y<sub>0.2</sub>O<sub>3-δ</sub> proton conductor densified at 1200 °C, *J. Mater. Chem. A*, **10** (2022) 4428–4439. <https://doi.org/10.1039/D1TA09998A>
69. Hocquet S, Dupont V, Cambier F, Ludewig F, et al., Densification of complex shape ceramics parts by SPS, *J. Eur. Ceram. Soc.*, **40**(7) (2020) 2586–2596. <https://doi.org/10.1016/j.jeurceramsoc.2019.10.038>
70. Paygin V, Dvilis E, Stepanov S, Khasanov O, et al., Manufacturing optically transparent thick zirconia ceramics by spark plasma sintering with the use of collector pressing, *Appl. Sci.*, **11** (2021) 1304. <https://doi.org/10.3390/app11031304>
71. Dvilis ES, Khasanov OL, Sokolov VM, Pokholkov JP, Method for compacting powder materials into articles and a mold for implementing the method. U.S. Patent No. 6,919,041, 19 July 2005. Russian Patent #2225280 (10.03.2004); Europatent No 1459823 (11.03.2009).
72. Cologne M, Rashkova B, Raj R, Flash sintering of nanograin zirconia in <5 s at 850 °C, *J. Am. Ceram. Soc.*, **93** (2010) 3556–3559. <https://doi.org/10.1111/j.1551-2916.2010.04089.x>
73. Bu J, Jonsson PG, Zhao Z, Dense and translucent BaZr<sub>x</sub>Ce<sub>0.8-x</sub>Y<sub>0.2</sub>O<sub>3-δ</sub> (x=0.5, 0.6, 0.7) proton conductors prepared by spark plasma sintering, *Scr. Mater.*, **107** (2015) 145–148. <https://doi.org/10.1016/j.scriptamat.2015.06.006>
74. Maekawa T, Kurosaki K, Yamanaka S, Thermal and mechanical properties of perovskite-type barium hafnate, *J. Alloys Compd.*, **407**(1–2) (2006) 44–48. <https://doi.org/10.1016/j.jallcom.2005.06.030>
75. Anselmi-Tamburini U, Buscaglia MT, Viviani M, Bassoli M, et al., Solid-state synthesis and spark plasma sintering of submicron BaY<sub>x</sub>Zr<sub>1-x</sub>O<sub>3-x/2</sub> (x = 0, 0.08 and 0.16) ceramics, *J. Eur. Ceram. Soc.*, **26** (2006) 2313–2318. <https://doi.org/10.1016/j.jeurceramsoc.2005.04.022>
76. Ricote S, Caboche G, Estournes C, Bonanos N, Synthesis, sintering, and electrical properties of BaCe<sub>0.9-x</sub>Zr<sub>x</sub>Y<sub>0.1</sub>O<sub>3-δ</sub>, *Journal of Nanomaterials*, **2008** (2008) 354258. <https://doi.org/10.1155/2008/354258>
77. Park HJ, Munir ZA, Kim ST, Grain boundary protonic conductivity in highly dense nano-crystalline Y-doped BaZrO<sub>3</sub>, *J. Korean Chem. Soc.*, **47** (2010) 70–71. <https://doi.org/10.4191/KCERS.2010.47.1.071>
78. Park HJ, Roh JW, Protonic conduction of nanostructured Y-doped BaZrO<sub>3</sub>, *Journal of Nanomaterials*, (2016) 8757305. <https://doi.org/10.1155/2016/8757305>
79. Wallis J, Urban L, Grimmer C, Bodnar W, Structural and electrical properties of BaZr<sub>0.7</sub>Ce<sub>0.2</sub>Y<sub>0.1</sub>O<sub>3-d</sub> proton conducting ceramic fabricated by spark plasma sintering, *Solid State Ionics*, **345** (2020) 115118. <https://doi.org/10.1016/j.ssi.2019.115118>
80. Simonenko TL, Kalinina MV, Simonenko NP, Simonenko EP, et al., Synthesis of BaCe<sub>0.9-x</sub>Zr<sub>x</sub>Y<sub>0.1</sub>O<sub>3-δ</sub>

nanopowders and the study of proton conductors fabricated on their basis by low-temperature spark plasma sintering, *Int. J. Hydrogen En.*, **44(36)** (2019) 20345–20354. <https://doi.org/10.1016/j.ijhydene.2019.05.231>

81. Wang D, Zhang Z, Song T, Sun H, et al., Synthesis of  $\text{BaZr}_{0.1}\text{Ce}_{0.7}\text{Y}_{0.2}\text{O}_{3-\delta}$  nano-powders by aqueous gel-casting for proton-conducting solid oxide fuel cells, *Int. J. Appl. Ceram. Technol.* **21** (2024) 299–310. <https://doi.org/10.1111/ijac.14497>

82. Kindelmann M, Escolastico S, Almar L, Vayyala A, et al., Highly conductive grain boundaries in cold-sintered barium zirconate-based proton conductors, *J. Mater. Chem. A*, **12** (2024) 3977–3988. <https://doi.org/10.1039/D3TA07076J>

83. Todd RI, Zapata-Solvas E, Bonilla RS, Sneddon T, et al., Electrical characteristics of flash sintering: thermal runaway of Joule heating, *J. Eur. Ceram. Soc.*, **35(6)** (2015) 1865–1877. <https://doi.org/10.1016/j.jeurceramsoc.2014.12.022>

84. Caliman LB, Bichaud E, Soudant P, Gouvea D, et al., A simple flash sintering setup under applied mechanical stress and controlled atmosphere, *MethodsX*, **2** (2015) 392–398. <http://dx.doi.org/10.1016/j.mex.2015.10.004>

85. Yoon B, Avila V, Lavagnini IR, Campos JV, et al., Reactive Flash Sintering of Ceramics: A Review, *Adv. Eng. Mater.*, **25** (2023) 2200731. <https://doi.org/10.1002/adem.202200731>

86. Ren K, Liu J, Wang Y, Flash sintering of yttria-stabilized zirconia: Fundamental understanding and applications, *Scripta Materialia*, **187** (2020) 371–378. <https://doi.org/10.1016/j.scriptamat.2020.06.040>

87. Steil MC, Marinha D, Aman Y, Gomes JRC, et al., From conventional ac flash-sintering of YSZ to hyper-flash and double flash, *J. Eur. Ceram. Soc.* **33** (2013) 2093–2101. <http://dx.doi.org/10.1016/j.jeurceramsoc.2013.03.019>

88. Francis JSC, Raj R, Influence of the field and the current limit on flash sintering at isothermal furnace temperatures, *J. Am. Ceram. Soc.*, **96(9)** (2013) 2754–2758. <https://doi.org/10.1111/jace.12472>

89. Du Y, Stevenson AJ, Vernat D, Diaz M, et al., Estimating Joule heating and ionic conductivity during flash sintering of 8YSZ, *J. Eur. Ceram. Soc.*, **36** (2016) 749–759. <http://dx.doi.org/10.1016/j.jeurceramsoc.2015.10.037>

90. Bai Y, Zhang Y, Tian Z, Zhang J, et al., Effect of current density on the microstructure and mechanical properties of 3YSZ/ $\text{Al}_2\text{O}_3$  composites by flash sintering, *Materials*, **15(9)** (2022) 3110. <https://doi.org/10.3390/ma15093110>

91. Muccillo R, Muccillo ENS, Kleitz M, Densification and enhancement of the grain boundary conductivity of gadolinium-doped barium cerate by ultra fast flash grain welding, *J. Eur. Ceram. Soc.*, **32** (2012) 2311–2316. <http://dx.doi.org/10.1016/j.jeurceramsoc.2012.01.032>

92. Cologna M, Francis SCJ, Raj R, Field assisted and flash sintering of alumina and its relationship to conductivity and MgO-doping, *J. Eur. Ceram. Soc.*, **31** (2011) 2827–2837. <https://doi.org/10.1016/j.jeurceramsoc.2011.07.004>

93. Karakuscu A, Cologna M, Yarotski D, Won J, et al., Defect structure of flash sintered strontium titanate, *J. Am. Ceram. Soc.*, **95** (2012) 2531–2536. <https://doi.org/10.1111/j.1551-2916.2012.05240.x>

94. Zapata-Solvas E, Bonilla S, Wilshaw PR, Todd RI, Preliminary investigation of flash sintering of SiC, *J. Eur. Ceram. Soc.*, **33** (2013) 2811–2816. <https://doi.org/10.1016/j.jeurceramsoc.2013.04.023>

95. Muccillo R, Kleitz M, Muccillo ENS, Flash grain welding in yttria stabilized zirconia, *J. Eur. Ceram. Soc.*, **31(8)** (2011) 1517–1521. <https://doi.org/10.1016/j.jeurceramsoc.2011.02.030>

96. Ahamer CM, Opitz AK, Rupp GM, Fleig J, Revisiting the temperature dependent ionic conductivity of yttria stabilized zirconia (YSZ), *J. Electrochem. Soc.*, **164** (2017) F790–F803. <http://dx.doi.org/10.1149/2.0641707jes>

97. Francis JSC, Cologna M, Raj R, Particle size effects in flash sintering, *J. Eur. Ceram. Soc.*, **32** (2012) 3129–3136. <http://dx.doi.org/10.1016/j.jeurceramsoc.2012.04.028>

98. Bhandari S, Mishra TP, Guillon O, Yadav D, et al., Accessing the role of Joule heating on densification during flash sintering of YSZ, *Scripta Materialia*, **211** (2022) 114508. <https://doi.org/10.1016/j.scriptamat.2022.114508>

99. Hao X, Liu Y, Wang Z, Qiao J, et al., A novel sintering method to obtain fully dense gadolinia doped ceria by applying a direct current, *J. Power Sources*, **210** (2012) 86–91. <https://doi.org/10.1016/j.jpowsour.2012.03.006>

100. Soleimany M, Paydar M, Investigation on flash sintering of  $\text{BaZr}_{0.1}\text{Ce}_{0.7}\text{Y}_{0.2}\text{O}_{3-d}$  compound; using nickel wire as electrode material, *Ceram. Int.*, **46** (2020) 2128–2138. <http://dx.doi.org/10.1016/j.ceramint.2019.09.196>

101. Grasso S, Sakka Y, Rendtorff N, Hu CF, et al., Modeling of the temperature distribution of flash sintered zirconia, *J. Ceram. Soc. Jap.*, **119** (2011) 144–146. <https://doi.org/10.2109/icersj2.119.144>

102. Wang S, Mishra TP, Deng Y, Kaletsch A, et al., Experimental and numerical studies of densification and grain growth of 8YSZ during flash sintering. *Adv. Eng. Mater.*, **25** (2023) 2201744. <https://doi.org/10.1002/adem.202201744>

103. Rybakov KI, Olevsky EA, Krikun EV, Microwave sintering: fundamentals and modeling, *J. Am. Ceram. Soc.*, **96** (2013) 1003–1020. <https://doi.org/10.1111/jace.12278>

104. Yu S, Gu Yu, Bi L, Microwave heating technology for electrolytes of solid oxide fuel cells, *Russ. Chem. Rev.*, **91(11)** (2022) RCR5061. <https://doi.org/10.57634/RCR5061>

105. Ćurković L, Veseli R, Gabelica I, Žmak I, et al., A review of microwave-assisted sintering technique. *Transactions of Famena XLV-I*, (2021). <https://doi.org/10.21278/TOF.451021220>

106. Leriche A, Hampshire S, Cambier F. Sintering of ceramics. Reference module in materials science and materials engineering. Elsevier, 2017, <https://doi.org/10.1016/B978-0-12-803581-8.10288-7>

107. Vanetsev AS, Orlov AV, Tretyakov YD, High density  $\text{BaCeO}_3$  ceramics sintered using microwave irradiation, *MRS Online Proceedings Library*, **906** (2005) 104. <https://doi.org/10.1557/PROC-0906-HH01-04>

108. Amiri T, Etsell TH, Sarkar P, Direct microwave sintering of poorly coupled ceramics in electrochemical devices, *J. Electrochem. Sci. Technol.*, **13(3)** 2022 390–397. <https://doi.org/10.33961/iectst.2022.00290>

109. Hussain A, Hassan M, Song R-H, Khan MZ, et al., Ultra-fast route to fabricate large-area anode-supported solid oxide fuel cell via microwave-assisted sintering, *Ceram. Int.*, **49(18)** 2023 30452–30460. <https://doi.org/10.1016/j.ceramint.2023.06.309>

110. Zhong Z, Xu X, Zhang Z, Li J, et al., *Int. J. Hydrogen En.*, **47(60)** (2022) 25367–25377. <https://doi.org/10.1016/j.ijhydene.2022.05.292>